Frontiers in Earth Science

TYPE Original Research
PUBLISHED 09 May 2023
DOI 10.3389/feart.2023.1182646

OPEN ACCESS

EDITED BY
Yunyan Ni,
China University of Petroleum, China

REVIEWED BY
Guodong Zheng,
China University of Geosciences at Wuhan, China
Min Wang,
China University of Petroleum, Huadong, China

*CORRESPONDENCE
Chaodong Wu,
cdwu@pku.edu.cn

RECEIVED 09 March 2023
ACCEPTED 17 April 2023
PUBLISHED 09 May 2023

CITATION
Jiao Y, Wu C, Zhou T and Wang J (2023), Episodic hydrothermal activities impact on organic matter enrichment in the post-collision rift basin of Permian Lucaogou Formation, southern Junggar Basin, NW China.
Front. Earth Sci. 11:1182646.
doi: 10.3389/feart.2023.1182646

Episodic hydrothermal activities impact on organic matter enrichment in the post-collision rift basin of Permian Lucaogou Formation, southern Junggar Basin, NW China

Yue Jiao[1], Chaodong Wu[1]*, Tianqi Zhou[2] and Jialin Wang[1]

[1]Key Laboratory of Orogenic Belts and Crustal Evolution, Ministry of Education, School of Earth and Space Sciences, Peking University, Beijing, China, [2]Research Institute of Petroleum Exploration and Development, PetroChina, Beijing, China

The factors controlling the organic matter accumulation in the organic-rich shale of the Lucaogou Formation in the southern Junggar Basin, remain controversial. To more explicitly reveal the hydrothermal events and its mechanism on the organic matter enrichment, we performed mineralogy and geochemistry methods on dolomite and black shale samples from Well FK-1 in Fukang Sag. The high (Fe + Mn)/Ti ratios, the enrichment of Ca, Mg, Fe, Mn, and REY, and multiple hydrothermal minerals (e.g., ankerite, dolomite, zeolite, authigenic albite, and microcline) suggest five episodes of hydrothermal events. In addition, the low-to-high-varied Sr/Ba, V/(V + Ni) (Al + Fe)/(Ca + Mg), and Sr/Cu ratios, as well as the dolomite formation all well indicate a brackish-saline, suboxic-anoxic, shallow to deep water condition under a warm-humid to hot-arid climate with rhythmic sedimentation. The fluctuated total organic carbon content (up to 12.16 wt%) suggest the periodic organic matter accumulation. Three patterns of organic matter enrichment occurred during the rift-drift transition of the southern Junggar Basin, productivity and preservation played distinguishing roles in different intervals. Productivity periodically fluctuated because of the episodic hydrothermal events and warm-humid climate changes. Preservation was triggered by the saline, anoxic, and well-stratified water setting under the relatively hot-arid climate, which became progressively favorable in the gradually stabilized basin.

KEYWORDS

organic-rich shale, hydrothermal events, paleoenvironment changes, rhythmic sedimentation, rift-drift transition

1 Introduction

The evolution of rift basins is linked to tectonic, sedimentary and magmatic processes worldwide (Wang et al., 2019d; Noori et al., 2019; Rubinstein and Carrasquero, 2019; Zhang et al., 2020d), and hydrothermal fluids play essential roles in these processes (Incerpi et al., 2020). Hydrothermal fluids from the lower crust and upper mantle usually carry multiple elements (e.g., Ca, Mg, Cu, Hg, P, S) that exist as cations and onions (German et al., 2006; Sherman et al., 2009). During the upward movement along faults and the water circulation in the basin (Yu et al., 2019; Negrete-Aranda et al., 2021), with the changes of temperature, pressure, pH, salinity and redox conditions, hydrothermal fluids deposit carbonate, quartz, Ca-Mg-siderite, sulfate, and sulfide (Renaut et al., 2002; Lima and De Ros, 2019; Renard et al., 2019; Yang et al., 2020; Renaut et al., 2021). The controlling factors on organic matter enrichment are primary productivity (e.g., plankton and bacteria), preservation of organic matter, and dilution and/or silicification effects of terrigenous detrital input (Tourtelot, 1979; Rimmer et al., 2004; Li et al., 2017a; Zou et al., 2019; Jiang et al., 2020; Xie et al., 2021). There are still different views on the mechanism of organic matter enrichment in post-collision rift basins (Hu et al., 2018; Li et al., 2020a; Wang et al., 2020a; Hadad et al., 2021; Xu et al., 2021). Hydrothermal events in rift basins can not only affect primary productivity by delivering abundant nutrient elements (e.g., N, P, Ba, Fe) (Gao et al., 2018; Cheng et al., 2020; Xie et al., 2021) and toxic elements (e.g., Cu, Cr, Hg) (Kadar et al., 2006; Han et al., 2011), but also increase the salinity and reducing conditions of the water column, and enhance the preservation (Payne and Egan, 2019; Zhang et al., 2020a; Liu et al., 2020; Tan et al., 2021).

The southern Junggar Basin, characterized by the rifting in the Permian and subsequent depression in the Triassic (Yu et al., 2016; Tang et al., 2021; Wang et al., 2021), contains organic-rich shale deposits and experienced the environmental evolutions of shallow marine-delta-shallow lacustrine systems in the Permian (Wang et al., 2018b). The Lucaogou Formation contains one of the most significant organic-rich sediments, which is mainly composed of dolomitic mudstone, tuffs, and oil shale (Hackley et al., 2016). The abundant dolomitic materials within the sequence are resistant to the compaction during diagenesis, whereas the organic acid produced during maturation can dissolve the former feldspar and dolomite particles, these resulted in better reservoir characteristics, making the Lucaogou Formation shale a primary exploration target for shale oil in northwestern China (Cao et al., 2016; Wu et al., 2016; Zhao et al., 2017; Zhang et al., 2018a; Pang et al., 2018). The U-Pb geochronology of the Lucaogou Formation is between 268 and 290 Ma (Zhang et al., 2015; Zhang et al., 2018d; Gao et al., 2020), and new research refines the age to 285–294 Ma, which belongs to the Artinskian epoch in the Early Permian (Sun et al., 2022). Synsedimentary magmatism were abundant around Carboniferous-Permian boundary times (~300 Ma) (Shu et al., 2011; Liu et al., 2012; Wang et al., 2019b), and hydrothermal activities in the Lucaogou Formation have been recorded as deposits in the southern Junggar Basin and its adjacent area, including the exhalative dolostone in the Santanghu Basin and phenocryst-like mineral assemblages in the eastern Junggar Basin (Li et al., 2017b; Li et al., 2021a). The most significant factors controlling the organic matter accumulation in the Lucaogou Formation is still under discussion: Liu et al. (2019a) suggested that semi-shallow and semi-saline lake water under the semi-humid climate enhanced organic matter preservation. Meng et al. (2022) and Tao et al. (2022) proposed that multiple volcanic-hydrothermal activities promoted algae blooming and triggered a saline, anoxic, stable-stratified water setting for organic matter enrichment. Jiao et al. (2020) suggested that mixed volcanic, hydrothermal, and lacustrine sediments were beneficial for hydrocarbon generation. Zhang et al. (2019a) and Cheng et al. (2022) considered that each factor, including terrestrial and tuffaceous inputs, redox conditions, and primary productivity, played a leading role in different intervals of deposition. Therefore, it is essential to study the hydrothermal activities, sedimentary settings, and the controlling factors of the organic matter enrichment in the Early Permian of the southern Junggar Basin, and results will also provide a favorable evidence to the shale deposition in rift basins globally.

The shale strata and its associated fine-grained interlayers containing petroleum is a self-contained and source-reservoir system, with diverse contents and maturities of organic matter (Wang et al., 2015; Wang et al., 2019c; Zhao et al., 2020b). Organic-rich shale usually refers to the shale with elevated total organic carbon contents (TOC) (generally >2%, Moore, 1969; Hosterman and Whitlow, 1981; Farrimond et al., 1989). Generally, the heterogeneity of the Lucaogou Formation reflects the complexity of petrology, mineralogy and geochemistry, which were affected by paleoenvironmental changes, tectonic settings and magmatic activities (Carroll, 1998). Multiple macroscopic methodologies (including mineralogical composition, elemental analysis, and the evolution of TOC in different system tracts) have been applied to the organic-rich shale in the Lucaogou Formation, and decipher the spatiotemporal variabilities of petrology, geochemistry, and stratigraphy (Gao et al., 2016; Zhang et al., 2016; Zhang et al., 2019a; Ren et al., 2019; Li et al., 2021a). Microstructural analyses on a single sample can reflect subtle fluctuations in the paleoenvironment recorded in shale laminae and wipe off the "whole-rock average effect". These microstructural methods consist of exploring the petrological fabric (Qiu et al., 2016a), QEMSCAN mineralogical distribution (Liu et al., 2019b), reconstructing pore structure using mercury injection capillary pressure (MICP) and X-ray computed tomography (CT) (Yang et al., 2019b; Wu et al., 2019), and micro-X-ray fluorescence (µXRF) mapping. Using µXRF mapping is beneficial for obtaining a high-resolution elemental distribution map, and this technique has been widely utilized in geological sediments (Frisia et al., 2012; Flude et al., 2017), diamond drill-cores (Potter and Brand, 2019), and paleontological fossils (Li et al., 2021b). Additionally, the mapping approach is effective on multimineral characterization, chemo-sedimentary facies analysis, and paleoenvironmental reconstruction of shale samples (Liu et al., 2019b; Mouro et al., 2020; Kim et al., 2021).

In this study, mineralogy and geochemistry analyses, including µXRF mapping and *in-situ* rare Earth elements tests, are conducted on core samples from Well FK-1 deposited in the Early Permian (Lucaogou Formation) in the Fukang Sag, southern Junggar Basin, to 1) describe the episodes and intensity of hydrothermal events, 2) decipher the process of paleoenvironmental fluctuation, and 3) illustrate the controlling effects of hydrothermal and paleoenvironmental changes on the organic matter enrichment.

2 Geological setting

The Central Asian Orogenic Belt (CAOB) is the largest Phanerozoic juvenile crustal growth orogenic belt in the world and is formed through the accretion of island arcs, ophiolites, and microcontinental fragments (Wang et al., 2018a). The triangular-shaped Junggar Basin is a part of the CAOB, with Kalamaili in the north and Bogda Mountains in the south (Figure 1A, modified after Wang et al., 2021). Rapid lateral facies and strata thickness changes with unique sedimentary characteristics in the Permian-Early Triassic sediments of the Bogda regions reveal that the southern and northern Bogda Mountains are located in different half-grabens and/or grabens (Wang et al., 2019b), and the thickness of

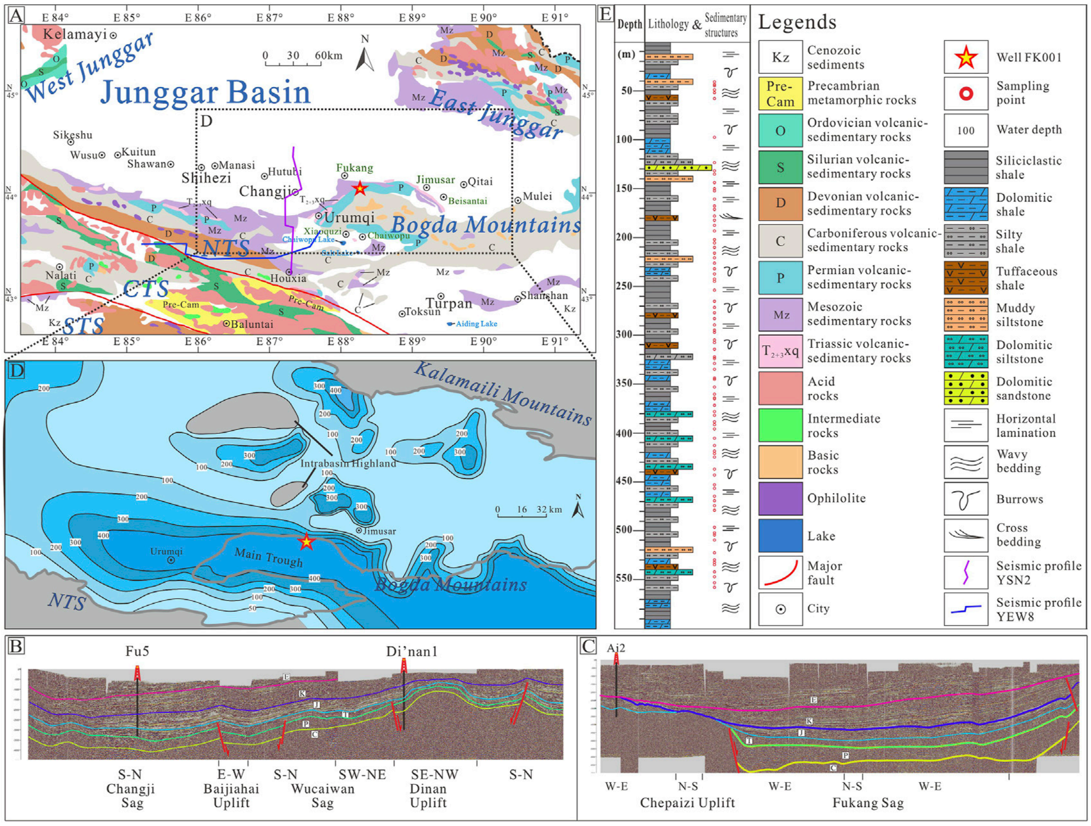

FIGURE 1
Geological map and structural framework of the study area. **(A)** Tectonic outlines of the southern Junggar Basin and its adjacement areas (modified after Wang et al., 2021). **(B)** Seismic profile YSN2 in Junggar Basin. **(C)** Seismic profile YEW8 in Junggar Basin. **(D)** Thickness of the Lucaogou Formation strata in the southern Junggar Basin. **(E)** Stratigraphic column of Well FK-1, Fukang Sag, the southern Junggar Basin.

the fine-grained lacustrine sediments close to the margin of the Bogda Mountains exceeds 1,000 m (Luo et al., 2018). The Permian strata in southern Junggar Basin comprises Shirenzigou, Tashikula, Wulabo, Jingjingzigou, Lucaogou, Hongyanchi, Quanzijie, and Wutonggou formations from bottom to top, recorded the arid climate in the Early Permian and the humid climate in the Middle-Late Permian (Gao et al., 2020). Compared with the Jingjingzigou and Hongyanchi formations, the Lucaogou Formation contains much higher TOC (up to 20%) and Hydrogen Index (HI) values (up to 800 mg/g. TOC) and exhibits better hydrocarbon potential in the southern Junggar Basin (Carroll, 1998; Qiu et al., 2016b; Chen et al., 2018; Luo et al., 2018; Wang et al., 2019c). The oil reservoir of the Lucaogou Formation is mainly distributed within the Bogda piedmont depression (including the Fukang Fault Belt, Beisantai Uplift, Xiaoquzi Area, and Chaiwopu Sag), the eastern edge of the Jimusar Sag in Junggar Basin (Tao et al., 2012; Cao et al., 2016; Liu et al., 2022a; Zheng et al., 2022), and the north margin of Turpan-Hami Basin (Song et al., 2018; Dang et al., 2019).

The Lucaogou Formation is a lacustrine fine-grained mixed sedimentary sequence (Liu et al., 2018; Wang et al., 2020b), with extensive distribution of alternating organic-rich shale, argillaceous dolomite, carbonate, tuff, and silt/sandstone (Qiu et al., 2016a). Maceral compositions includes algal detritus, liptodetrinite, vitrodetrinite and inertodetrinite (Tao et al., 2012; Xie et al., 2015; Li et al., 2019; Zheng et al., 2022). These all indicate a semi-deep to deep lacustrine setting and a long-distance transport of the original macerals. Provenance analyses revealed the low-order cycle of sediments from the surrounding paleo-uplift (Li et al., 2016; Peng, 2016; Zha et al., 2021) and the weak-moderate chemical weathering of the parent rocks (Tao et al., 2017; Liu et al., 2020) in the Early Permian, which resulted in the heterogeneity of thickness and hydrocarbon potential in the Lucaogou Formation strata (Li et al., 2020b). Taking the maximum flooding surface as a boundary, the Lucaogou Formation was divided into two members upward (Cao et al., 2016). Compared with the lower member, the upper member contains higher TOC content and is more oil-prone (Hu et al., 2017). Because of the rapid subsidence under regional tectonic extension (Qiu et al., 2016b; Figures 1B, C), the Lucaogou Formation in the southern Junggar Basin has a maximum thickness of over 300 m in the Jimsuar Sag (Lin et al., 2021) and of over 500 m in the Fukang Sag, which is located near the main trough of the basin (Figure 1D).

3 Material and methods

The core samples obtained in this study are from the Well FK-1 (Figure 1) in the Fukang Sag, with a total cumulative thickness of 600 m. The drill cores cover the upper part of the Lucaogou

Formation (Figure 1E), and the serial numbers and depths of these samples are listed in Supplementary Table S1. These core samples were cut into 2-mm-thick slices using a diamond wire saw, and the cutting direction was perpendicular to the depositional bedding.

3.1 Mineralogy analyses

Thin sections were observed using an upright microscope (Nikon Eclipse E200, Japan). Hand specimen observations were performed using a scanning electron microscope (SEM, FEI Quanta 650 FEG, United States) at the School of Earth and Space Sciences, Peking University. The X-ray diffraction (XRD) of 39 powdered samples was performed using an X'Pert3 powder diffractometer (PANalytical B.V., Almeo, Netherlands) at the College of Chemistry and Molecular Engineering, Peking University. The carbonate content of 81 samples was measured by the carbonate content analyzer (GMY-2, China). Briefly, 50 mg of the bulk-rock powder reacted with an excess of 10% HCl in a closed system, and the released CO_2 was collected using a barometer. Pure calcite (99.9% carbonate content) was used as the standard sample.

3.2 Geochemistry analyses

Major and trace element contents were measured on 82 surface-polished samples using a portable X-ray fluorescence analyzer (Thermo Fisher Scientific Niton XL3t, United States) with a scanning radius of 4 mm. Each sample was scanned 3 times encompassing different laminae and areas of the surface-polished slices, which could be more representative for variable paleoenvironmental changes. Paleoenvironmental proxies including Sr/Ba, V/(V+Ni), (Al+Fe)/(Ca+Mg), Sr/Cu, Ba/Al, and (Fe+Mn)/Ti were calculated according to these data.

The μXRF mapping and *in-situ* rare Earth elements (REEs) tests were conducted on two samples, which perform hydrothermal characteristics. The μXRF mapping data were obtained using an M4 Tornado μXRF instrument (Bruker, Germany). Each sample was analyzed for more than 8 h, with an accuracy of 20 μm; further details have been described by Lin et al. (2021). The *in-situ* REEs test was acquired using the Thermofisher Scientific iCapRQ quadrupole-inductively coupled plasma-mass spectrometer (Q-ICP-MS) coupled with a 193 nm GeoLas HD laser-ablation (LA) system at the School of Earth and Space Sciences, Peking University. NIST SRM 610 and 612 were used as external standards, and the data were normalized by NASC (North American shale composite, Haskin et al., 1966) standard.

For TOC content determination, 50 mg clean powdered samples were heated gradually in the atmosphere of nitrogen, the amount of pyrolyzate released from kerogen was normalized to TOC to obtain the hydrogen index (HI), using the ELTRA CSi elemental analyzer at the Research Institute of Petroleum Exploration and Development, PetroChina, further details are described in Liu et al. (2017a) and Pang et al. (2018).

4 Results

4.1 Mineralogical characteristics

The lithology and geochemistry characteristics of samples in Well FK-1 exhibit complexity and particularity. The core samples consist of siliciclastic shale, dolomitic shale, silty shale, tuffaceous shale, muddy siltstone, dolomitic siltstone, and dolomitic sandstone, and present different sedimentary structures (Figure 1E). In tuffaceous shale samples, tuff, which is dominated by irregular feldspars, calcite, glass fragments, and clay minerals (Norin, 1955; Wu et al., 2022), present in the form of brown laminae, whereas rhmboic ankerite aggregate as bubble-like structures (Figures 2A–D). Silty shale samples show ZnS and TiO_2, and ankerite was intercalated with chlorite (Figures 2E, F). Hydrothermal minerals, including zircon, monazite grains, and fibrous mordenite are recognized in siliciclastic shale and dolomitic shale (Figures 2G–I). Siliciclastic shale present horizontal bedding and framboid pyrite (Figures 3A, C); whereas dolomitic siltstone exhibit wavy bedding and abundant dolomite, these demonstrate diverse water settings in the Early Permian (Figures 3D–F). Under fluorescent light, the green-brown laminalginite and sporinite are observed in siliciclastic shale and silty shale, respectively, whereas abundant organic matter exist in forms of amorphous structure and laminae (Figures 2F, H, Figure 3).

The mineralogical compositions of the 39 samples based on the XRD results are shown in Supplementary Table S2, the sum of the mineral percentage in each sample is about 100. The main mineralogical composition of samples are shown in Figure 4. Most of the samples are enriched in minerals associated with hydrothermal activities, including albite (10.3%–65.8%, avg. 40.2%), microcline (6.1%–61.1%, avg. 27.8%), and zeolite (1%–38.3%, avg. 17.5%). Carbonate content of the 81 samples varies from 2.27 wt% to 68.87 wt% (avg. 19.33 wt%) (Supplementary Table S3), and mainly comprise dolomite (12.3%–55.5%, avg. 29.6%) and ankerite (18.7%–44.2%, avg. 30.3%) according to the XRD results. Quartz and orthoclase are also abundant, whereas feldspar, sanidine, anorthite, analcime, pyrite, and siderite are rare in the samples.

4.2 Element compositions

The major element concentrations of the shale samples are presented in Supplementary Table S4; Figure 5. Ti, Al, K, and Si exhibit similar variation trends, which indicate periodic terrigenous input; whereas Ca and Mg curves present parallel variations with the (Fe+Mn)/Ti curve (Figure 7). Besides, Fe (1.25–19.64 wt%, avg. 2.86 wt%), P (0.03–3.31 wt%, avg. 0.22 wt%), and S (0.03–33.29 wt%, avg. 0.56 wt%) present low contents in most of the samples and extremely high values in few samples, indicating correlations with hydrothermal inputs. The trace element contents of the samples are summarized in Supplementary Table S5; Figure 6. The abundances of Sr, Ba, and Ni show correlations with salinity and redox condition; whereas Mn, Cr, Zn, and Zr varies strongly in several intervals, presenting correlations with (Fe + Mn)/Ti curve (Figure 7). The values of Th and U exhibit low values mostly and

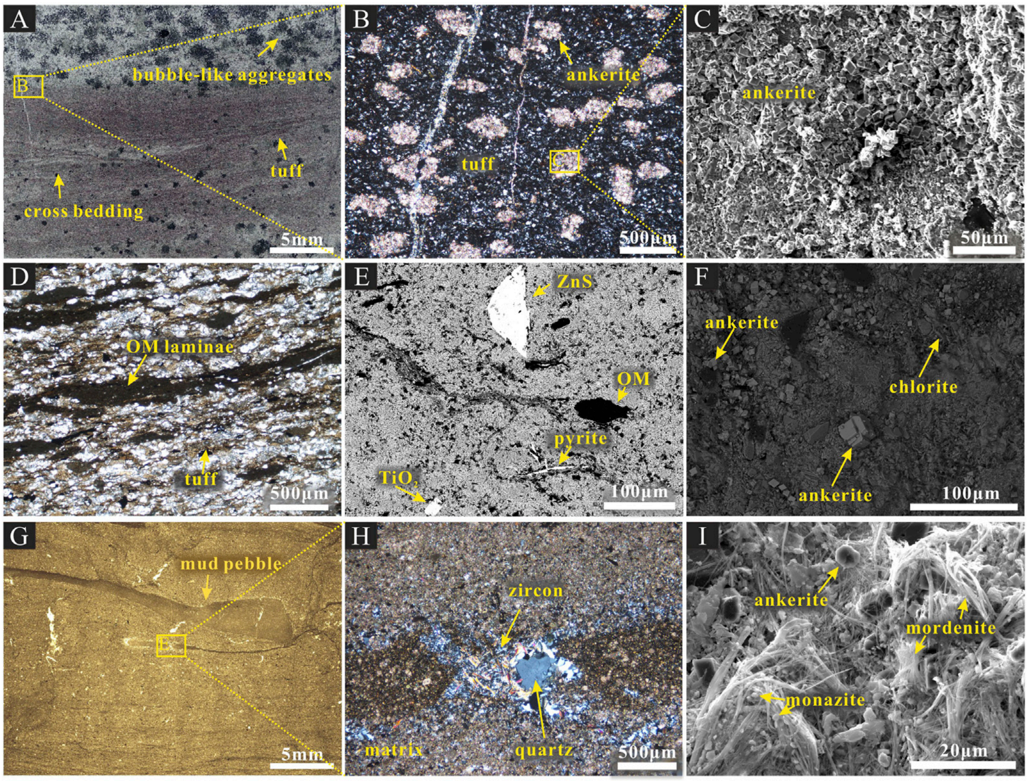

FIGURE 2
Microscopic characteristics of hydrothermal activities in shale samples of Well FK-1. **(A)** PL, F1-18, continuous photo presented cross-bedding, brown tuff laminae and bubble-like aggregates of ankerite. **(B)** XL, F1-18, tuff and bubble-like aggregates of ankerite. **(C)** SEM, F1-18, abundant rhombic ankerite. **(D)** PL, F1-6, tuff and organic matter laminae. **(E)** SEM, F1-39, ZnS, TiO_2, and pyrite indicated hydrothermal effects. **(F)** SEM, F1-64, chlorite intercalated with ankerite. **(G)** PL, F1-36, continuous photo presented hydrothermal intrusion which damaged the former mud pebble and left fibrous zircon. **(H)** XL, F1-36, fibrous zircon and quartz. **(I)** SEM, F1-78, anhedral ankerite, monazite grains, and fibrous mordenite illustrated hydrothermal precipitaion. Abbreviations: PL: plane-polarized light; XL: cross-polarized light; SEM: scanning electron microscope. Samples F1-6, F1-18, F1-36, F1-39, F1-64, and F1-78, at depths of 58.1, 181.6, 289.1, 305.3, 443.05, and 534.88 m, respectively.

extremely high values in a few samples, whereas Rb, V, and Cu varies indistinctively. Paleoenvironmental proxies of 82 samples are calculated based on the major and trace element concentrations, presenting rhythmic variations of paleoenvironment (Figure 7), as listed in the Supplementary Table S6.

The μXRF elemental mapping of sample F1-18 (tuffaceous shale, at a depth of 181.6 m) is divided into three groups based on specific elemental enrichment (Figure 8): i) dark particles at the top and middle areas are enriched with Cu, Fe, Mg, Mn, Zr, and Rb; ii) bright particles in the middle area, where Fe and S prevailed; and iii) the rest of the muddy part with wavy bedding containing abundant Al, Ca, Ba, K, P, Si, Sr, and Y. The μXRF elemental mapping of sample F1-78 (dolomitic shale, at a depth of 534.88 m) is divided into four groups based on specific element enrichment (Figure 9): i) yellow and ii) dark mud spread in turns over the sample, with enriched Al, Ba, Cu, Si, Ti, and V, and multiple K, and Mn, respectively; iii) bright particles in the middle part, where Co, Fe, S, and Zn prevailed; and iv) branch-like structures in the lower and upper-right parts of the sample, where Ca, Mg, Ni, Sr, Y, and Zr exhibit extremely high values. The *in-situ* REY data and the NASC-normalized value of samples F1-18 and F1-78, are listed in Supplementary Table S7. The samples are enriched in La, Ce, Nd, and Y.

4.3 TOC contents and HI values

The TOC contents of the 81 samples range from 0.29 wt% to 12.16 wt% (avg. 2.96 wt%), presenting rhythmic upwardly increasing trends in three intervals (at depths of 135–240 m, 280–400 m, and 420–540 m, respectively), and reach the maximum value in sample F1-10 (at a depth of 136.6 m). The HI values of 81 samples vary from 52 to 953 mg/g. TOC (avg. 410 mg/g. TOC), implying that the source rocks are mainly oil-prone and possess high hydrocarbon generation potential (Carroll et al., 1992; Luo et al., 2018; Zhang et al., 2020b; He et al., 2022; Figure 7; Supplementary Table S8).

5 Discussion

5.1 Episodic hydrothermal activities and their significances in the early Permian

Frequent hydrothermal activities in the Early Permian have been demonstrated by high $^{87}Sr/^{86}Sr$ values in tuffaceous shale (Li et al., 2021a), the absence of β-carotane (Wang et al., 2022), and negative

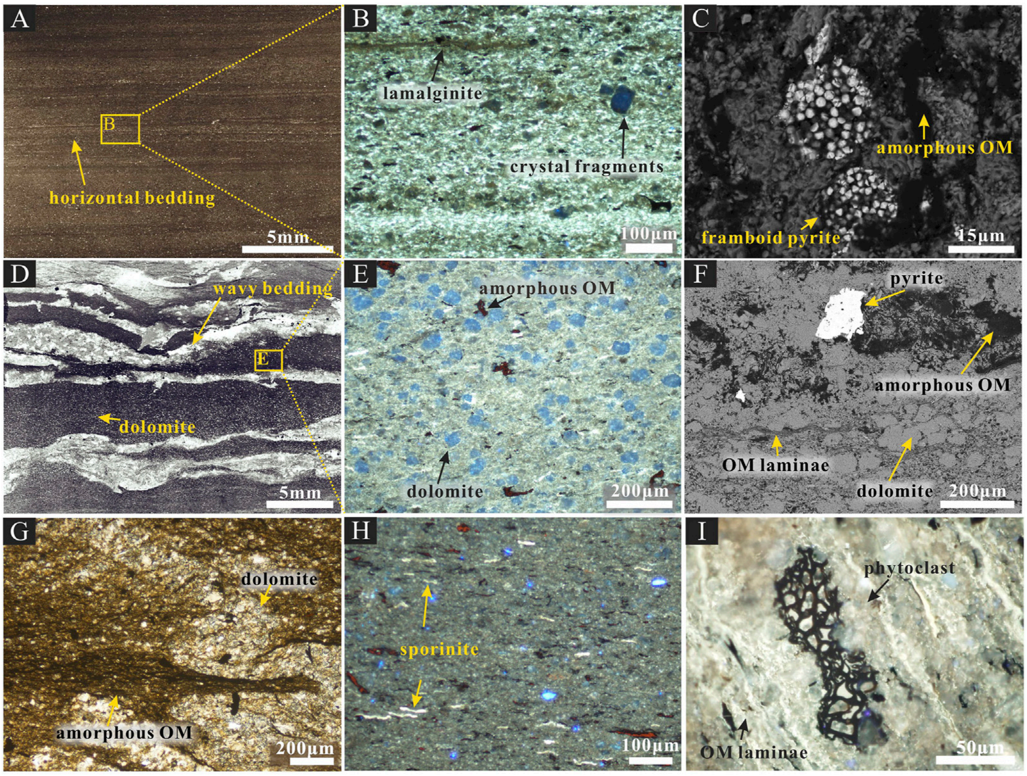

FIGURE 3
Microscopic characteristics of diverse water settings and various types of organic matter in shale samples of Well FK-1. **(A)** PL, F1-10, continuous photo showed the horizontal bedding, representing a low-energy water setting. **(B)** FL, F1-10, crystal fragments and lamalginite. **(C)** SEM, F1-10, framboid pyrite, and amorphous OM. **(D)** PL, F1-79, continuous photo presented the wavy bedding and abundant dolomite, which represented a shallower agitated water setting. **(E)** FL, F1-79, dolomite and amorphous OM. **(F)** SEM, F1-79, pyrite, abundant dolomite, organic matter laminae, and amorphous OM. **(G)** PL, F1-2, amorphous organic matter and dolomite. **(H)** FL, F1-33, sporinite. **(I)** PL, F1-63, phytoclast and OM laminae. Abbrieviations: PL: plane-polarized light; FL: fluorenscent light. OM: organic mater. Samples F1-2, F1-10, F1-33, F1-63, and F1-79, at depths of 44.4, 136.6, 271.1, 437.4, and 542.38 m, respectively.

$\delta^{18}O$ values of dolomite (Zhang et al., 2020a; Jiao et al., 2020). The gabbro porphyrite and rhyolite in Lucaogou Formation own zircon U-Pb ages of 288–297 Ma, indicating synsedimentary volcanic activities in the rift-drift transition background (Shu et al., 2011; Wang et al., 2019a; Zhao et al., 2020a; Sun et al., 2022).

5.1.1 Hydrothermal intensity

The ternary diagram of Fe vs. Mn vs. (Co + Ni + Cu) × 10 has been utilized to distinguish the hydrothermal input during deposition (Bonatti, 1975; Zeng et al., 2012; He et al., 2016; Zhang et al., 2018c). Most of the samples in Well FK-1 fall in the hydrothermal field, and several samples show properties common with Red Sea hydrothermal sediments (Figure 10), suggesting that samples in Well FK-1 received multiple hydrothermal inputs during the Lucaogou Formation.

Al and Ti are known to be affiliated with aluminosilicate phases and act as excellent indicators of terrigenous input, whereas Fe and Mn are often enriched in hydrothermal sedimentation (Baturin, 2012; Li et al., 2018; Lu et al., 2019). Therefore, the (Fe + Mn)/Ti ratio is an effective indicator of hydrothermal input, with values greater than 15 indicating typical hydrothermal sedimentation (He et al., 2016; Peng, 2016). In Well FK-1, the (Fe + Mn)/Ti ratios range from 4.78 to 119.72 (avg. 14.8) and present five positive excursions, which may refer to at least five episodes of hydrothermal events during deposition, these hydrothermal events are marked as transparent horizontal stripes and exhibit different characteristics (Figure 7). Upward, the first episode of hydrothermal events occurred at a depth of 495–545 m, with the enrichment of Ca, Fe, Mg, P, and S; the second episode appeared at a depth of 415–475 m, with an increase in Ba, Ca, and Mg; the third episode occurred at a depth of 270–400 m and was the greatest episode during the deposition, with the enrichment of Ba, Ca, Mg, Sr, Zn, and Zr; the fourth episode appeared at a depth of 135–255 m and was accompanied with abundant Ba, Fe, Mg, Ni, and V; and the fifth episode occurred at a depth of 40–70 m, with an increase in Ca, Fe, Mg, Mn, and V content (Figures 5, 6).

5.1.2 Hydrothermal characteristics

(1) Mineralogical associations with hydrothermal activities

Minerals discovered in the Lucaogou Formation consist of silica and siliceous minerals (including quartz, feldspar, orthoclase, albite, and plagioclase), clay minerals (smectite, illite, and chlorite), carbonate (including dolomite, calcite, ankerite, and siderite), zeolite (including analcime), pyrite, buddingtonite, chalcedony, halite, anhydrite, and glauberite (Liu et al., 2017a; Zhang et al.,

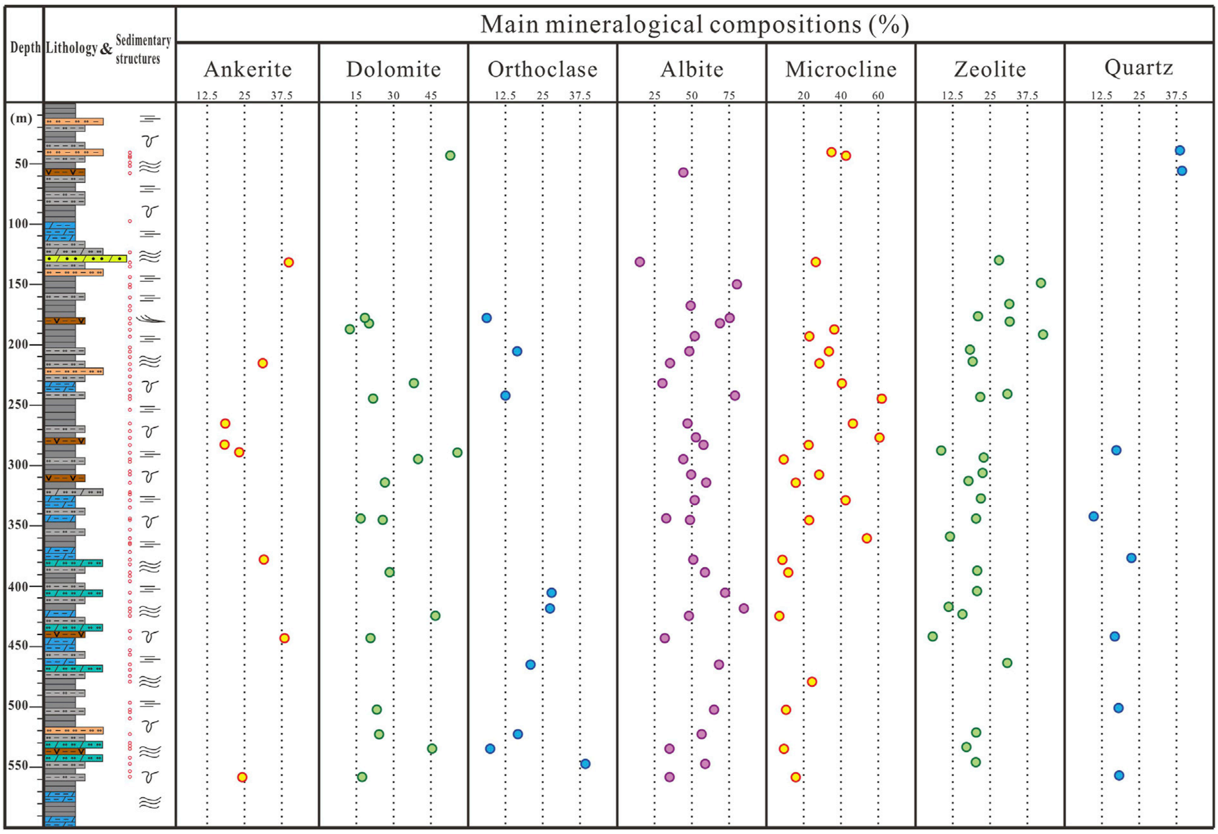

FIGURE 4
Main mineralogical compositions (%) of shale samples in Well FK-1. Most of the samples are enriched in ankerite, dolomite, albite, microcline, zeolite.

2018c; Yang et al., 2019a; Zhang et al., 2020d; Jiao et al., 2020; Lin et al., 2021). The second member of the Lucaogou Formation is mainly composed of non-clay siliceous minerals and carbonate minerals with extremely low clay content (Zhang et al., 2021), and the coexistence of strontianite and barite in the Lucaogou Formation of the Santanghu Basin provides mineralogical evidence for hydrothermal activities (Zhang et al., 2018c). According to the XRD results, samples in Well FK-1 present superior enrichment of albite (10.3%–65.8%, avg. 40.2%), microcline (6.1%–61.1%, avg. 27.8%), and zeolite (1%–38.3%, avg. 17.5%), which are reported to be formed in hydrothermal or volcanic systems (Chao et al., 1997; Abdullahi et al., 2017; Yang et al., 2019a; Yang et al., 2020; Zhang et al., 2020c), and present close correlations with hydrothermal intensity (Figure 7). Authigenic albite is believed to be correlated with syngenetic hydrothermal processes within paleolake or syn-rift deposits (Incerpi et al., 2020; Wu et al., 2022) and indicates a feldspar-dominated source accompanied by orthoclase in the former lagoonal environment (Brockamp and Clauer, 2013; Jiao et al., 2020).

Dolomitization in the Lucaogou Formation was correlated with synsedimentary hydrothermal activities at the lake bottom within an intracontinental rift basin (Zhang S. et al., 2020) and could be related to sufficient Mg supply and intense evaporation in shallow saline depositional environments (Yang et al., 2019a). The abundant rhomboid ankerite in F1-18 (Figures 2B, C) is surrounded by tuff (Figures 2A, B), resembling the sucrosic dolomite (D2 type) noted by Yang et al. (2019a) and subhedral dolomite noted by Wu et al. (2022). These observations indicate synsedimentary hydrothermal activities because ankerite mainly occurs in tuffs (Jiao et al., 2020). The coexistence of ankerite and chlorite in sample F1-64 can be another proof of distinctive hydrothermal events because the formation of chlorite is generally associated with low temperatures (<80°C) and Fe^{3+}- and Mg^{2+}-rich environments (Liu et al., 2019d). Therefore, subaqueous hydrothermal fluids with extremely high Fe and Mg contents (Figure 6) intruded into the basin, produced enormous explosions (Jiao et al., 2018), and boiled the bottom water, leaving bubble-like aggregates of rhomboid ankerite (Figures 2A, B) in the former sediments with cross-bedding (Figure 2A).

(2) Elemental enrichment in hydrothermal inputs

Synsedimentary hydrothermal activities can bring abundant eutrophic elements (e.g., N, P, and K) and metal elements (e.g., Ca, Mg, and Fe) into the bottom water and affect the chemical composition of the water column (Zhang et al., 2020b; Pan et al., 2020), and trace elements including Ni, Cu, Zn, Zr are generally more abundant in the hydrothermal deposits than in normal pelagic sediments (Bonatti, 1975; Loukola-Ruskeeniemi and Heino, 1996; Huang et al., 2019). Samples F1-36 and F1-39 are located in the

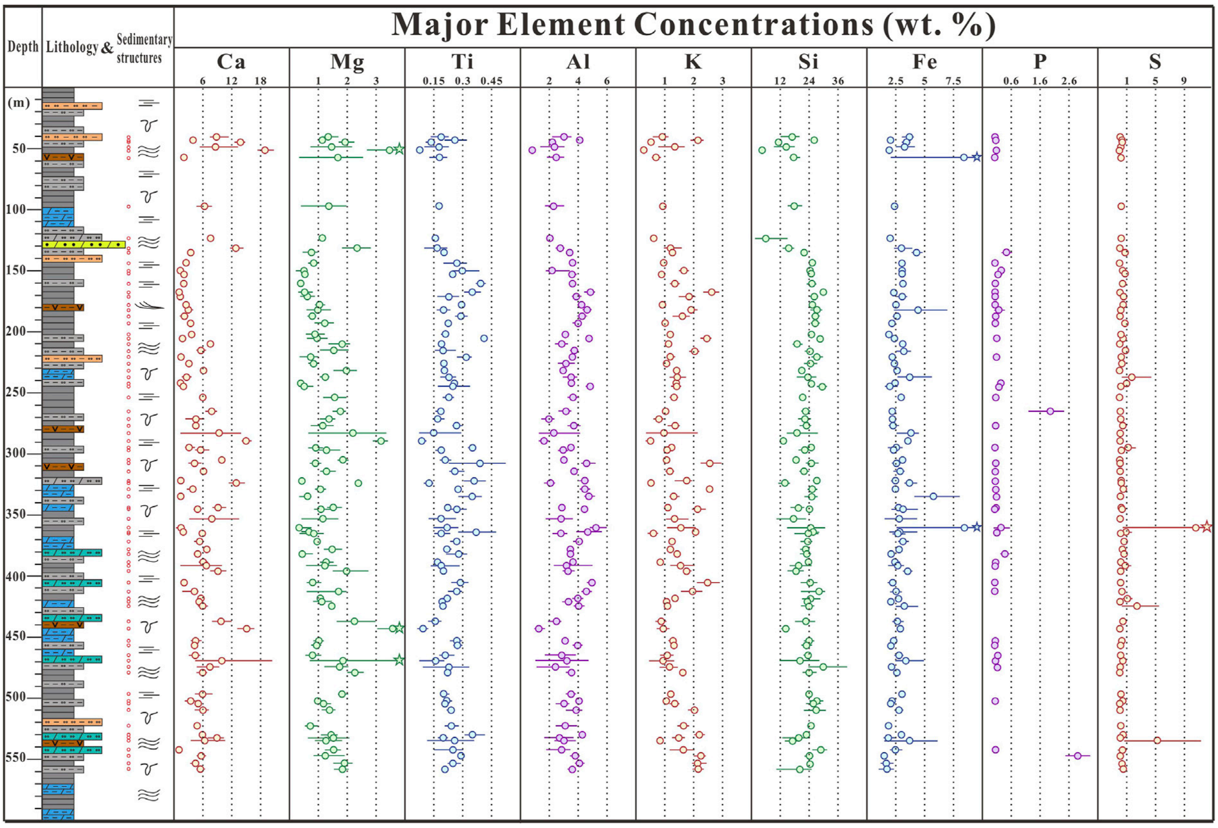

FIGURE 5
Major element concentrations (wt%) of shale samples in Well FK-1. The star symbol represented values which exceeded the boundary value.

range of the greatest positive excursion of the (Fe + Mn)/Ti curve. During this time, strong hydrothermal fluids damaged the former mud pebble (Figure 2G), and left ZnS (Figure 2E), fibrous zircon (Figure 2H), owing to the release of Zr and Zn during the hydrothermal intrusion, and the affinity of Zn and sulfide phases (Bonatti, 1975; Malisa, 2003; Jiao et al., 2019).

The µXRF mapping has been utilized in shale samples of the Lucaogou Formation because of the effectively elemental composition evalution (Liu et al., 2019a; Lin et al., 2021). The µXRF mapping results of samples F1-18 and F1-78 exhibit different features (Figures 8, 9). Specifically, in sample F1-18, hydrothermal fluids boiled the bottom water and formed bubble-like ankerite aggregates (Figure 2A), leaving abundant nutrients including Fe, Mg, Mn, Ba, P, and Sr (Figure 8), then diffused in the water column and delivered nutrients upward (Yang et al., 2020); the enriched S (Figure 8) illustrated an anoxic HS^- -rich water setting, which benefited organic matter preservation, and may be enhanced by hydrothermal activities (Meunier et al., 1987; Orberger et al., 2005; Liu et al., 2020). In sample F1-78, the i) branch-like structure filled with Ca, Mg, Ni, Sr, Y, and Zr and ii) bright particles with multiple Co, Fe, S, and Zn, suggesting hydrothermal infiltration into the surrounding sediments, which left specific elements along its track; whereas the iii) yellow and dark mud, enriched with Ba, Cu, and Mn, indicating that hydrothermal fluids enhanced water circulation and transferred nutrients to surface water.

The REE and yttrium (REY) concentrations, complexed by SO_4^{2-} and Cl^- ions at moderate (~100°C) and high temperatures (Douville et al., 1999), are highly correlated with hydrothermal fluids (Dai et al., 2016) and present different characteristics in samples F1–18 and F1–78 (Figures 8, 9). Specifically, sample F1–18 has Y enrichment in the bottom muddy part (Figure 8), whereas sample F1–78 not only presents Y enrichment in the upper-right part of the sample (Figure 9), but also shows the enrichment of La, Ce, Nd (Supplementary Table S7), which exist in the form of monazite with a diameter of 1–3 µm, and are attached to the fibrous mordenite (Figure 2I). Considering that the magma chamber presented at a shallow depth underneath the Santanghu area (Jiao et al., 2018), it can be concluded that the fractures resulting from rifts in the Junggar area connected lake water with the underneath magma chamber (Jiao et al., 2020). The mantle-derived hydrothermal fluids, supported by the $^{87}Sr/^{86}Sr$ values of dolomite (Zhang et al., 2020c), delivered abundant REY into the bottom water.

5.2 Paleoenvironmental variation indicators during the early Permian

5.2.1 Paleoclimate

Paleoclimate can greatly influence marine productivity, redox conditions, and the supply of terrestrial materials (Tan et al., 2021). The release of CO_2 from volcanic eruptions can create a

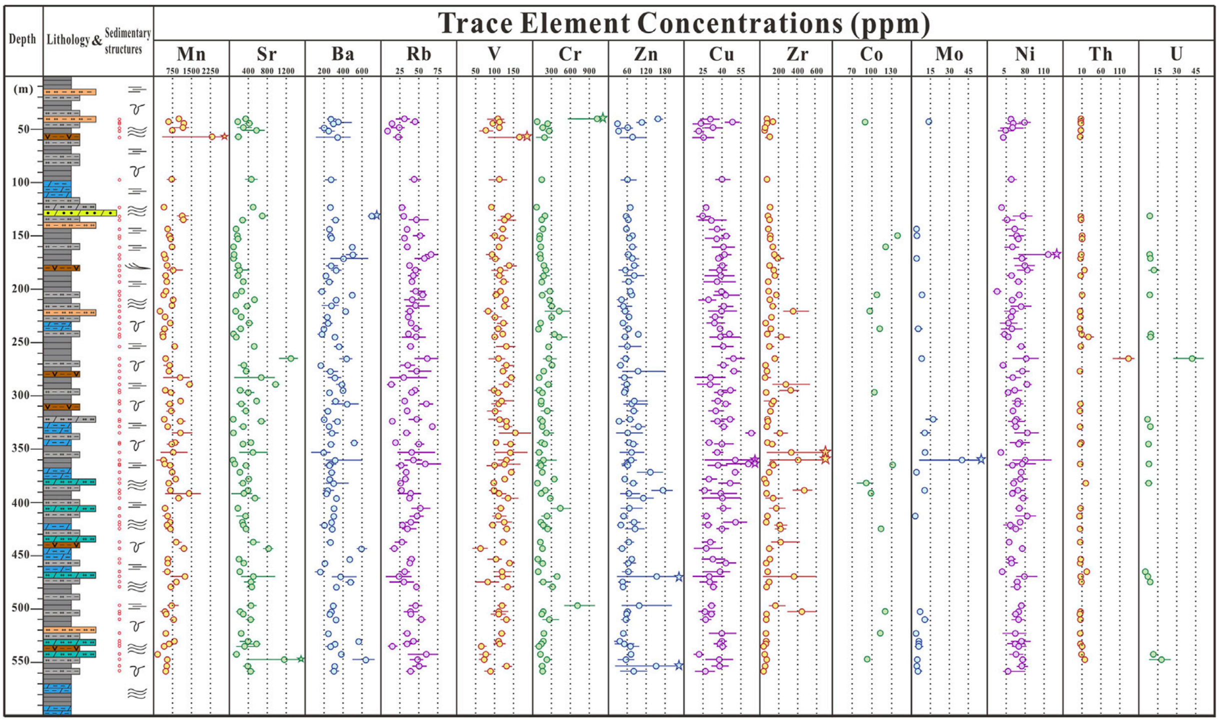

FIGURE 6
Trace element concentrations (ppm) of core samples in Well FK-1. The star symbol represented values which exceeded the boundary value.

"greenhouse" around the basin and promote the aridity (Qu et al., 2019; Pan et al., 2020). Abundant Sr reflects an arid climate with higher salinity, whereas a high Cu content indicates a moist climate with lower salinity (Liu et al., 2019b); therefore the ratio of Sr/Cu is a paleoclimate indicator, with 1.3 < Sr/Cu < 5 indicating a warm and humid climate, and Sr/Cu > 20 indicating a hot and arid climate (Zhang et al., 2018b). The Sr/Cu values (0.91–55.96, avg. 11.31) in Well FK-1 (Figure 7) suggest the rhythmic climatic variations between warm-humid and hot-arid climates. In addition, Wu et al. (2016) and Liu et al. (2019b) suggested abundant dolomite in the Lucaogou Formation depostied under an arid climate with significant surface evaporation. The carbonate content (2.27–68.87 wt%, avg. 19.33 wt%) in Well FK-1 shows coincident trends with Ca, Mg, Sr/Cu, Sr/Ba, and (Fe+Mn)/Ti curves, suggesting that because of the drop of temperature and pressure in the upward migration of hydrothermal fluids, the solubility of Ca and Mg decreased, abundant carbonate, especially dolomite, precipitated in the high saline water under an arid climate.

5.2.2 Paleosalinity

The salinization of the water column in the lacustrine basin can remarkably influence biological processes and mineral precipitation (Zhang et al., 2018c), which can be responses to dry-hot climate (Sun et al., 2013; Zhang et al., 2020d) and hydrothermal inputs (Zhang et al., 2020b). High saline water can form a stable density and salinity stratification (Qiu et al., 2016b): the less saline surface water containing abundant dissolved oxygen is conducive to algal, planktonic, and bacterial blooming (Wu et al., 2016); whereas the high saline bottom water benefits organic matter preservation (Liu et al., 2019b).

Being members of trace metallic elements in Group 2 (IIA; alkaline earths), Sr and Ba can be mainly delivered by riverine inputs, and own residence time in seawater of 2.4 Myr and 11 kyr, respectively (Wei and Algeo, 2020). With the increase of salinity and sulfate ion concentration, Ba precipitates in the form of barium sulfate before Sr can (Liang et al., 2014; Jiang et al., 2015). Therefore, Sr/Ba is considered to be a valid indicator of paleosalinity (Zhang et al., 2014; Liu et al., 2019b; Pan et al., 2020), with Sr/Ba <0.2 indicating fresh water, 0.2 < Sr/Ba <1.0 indicating brackish water, and Sr/Ba >1.0 indicating salt water (Zhang K. et al., 2020; Pan et al., 2020; Wei and Algeo, 2020; Liu et al., 2022a; Yang et al., 2022). The Sr/Ba ratios (0.13–3.36, avg. 1.21) in Well FK-1 suggest a mostly brackish-saline water setting with rhythmic variations. Furthermore, the high saline and stratified water column containing strongly reducing bottom waters can reduce the degradation of organic matter (Pratt, 1984; Jia et al., 2013; Shang et al., 2015; Liu et al., 2017a; He et al., 2018), therefore the similar trends of Sr/Ba and V/(V + Ni) curves and their high values at depths of 130–160 m and 280–320 m indicate good preservation of organic matter during these intervals.

5.2.3 Redox conditions

Redox conditions play a vital role in the alteration, paragenesis and precipitation of variable-valence elements (Stashchuk, 1972; Vovk, 1987), and are essential for organic matter degradation and preservation (Ding et al., 2019; Qu

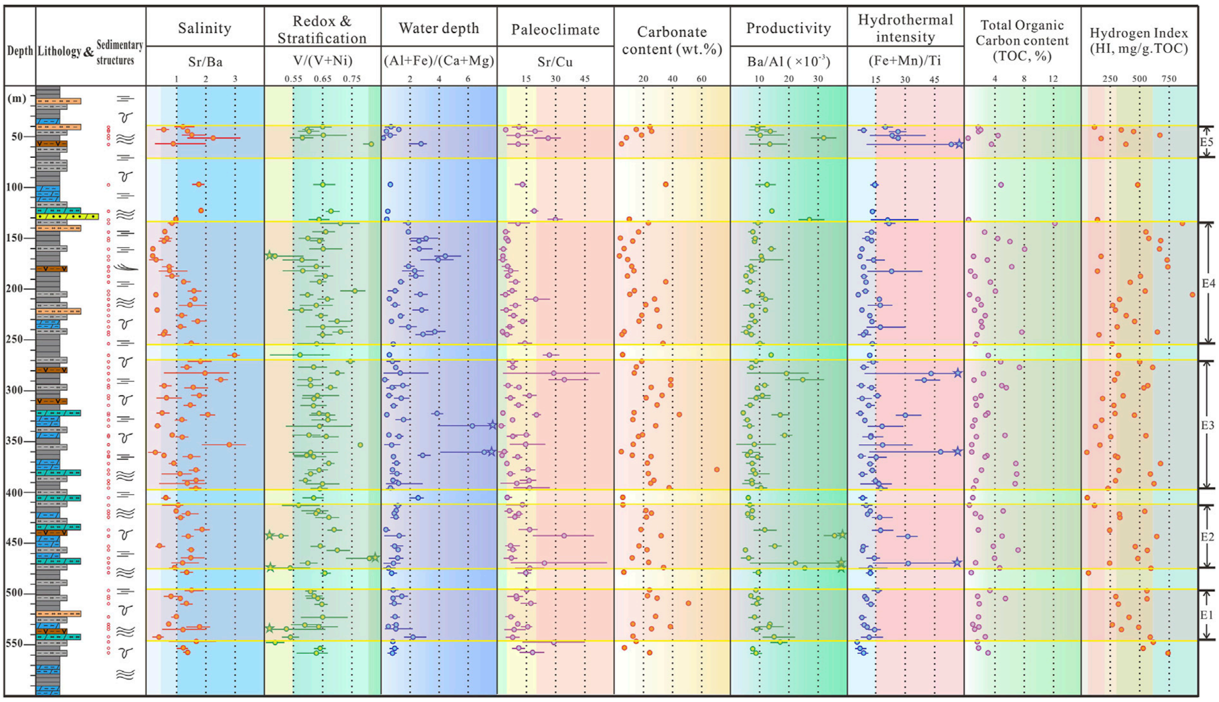

FIGURE 7
A comprehensive profile of lithology and paleoenvironmental proxies in Well FK-1. The Sr/Ba, V/(V + Ni) (Al + Fe)/(Ca + Mg), carbonate content, and Sr/Cu data suggest a brackish-saline, suboxic-anoxic, semi-deep to deep water setting in a warm-humid to hot-arid climate with rhythmic sedimentation. The TOC, HI, and Ba/Al contents present the periodic organic matter enrichment. Five episodes of hydrothermal events are marked as transparent horizontal stripes based on the (Fe + Mn)/Ti values. E1, E2, E3, E4, and E5 are abbreviations of the first, second, third, fourth, and fifth episode of hydrothermal events. The star symbol represent values which exceed the boundary value, and the discrimination criteria for each indicator are marked by vertical stripes.

et al., 2019). Redox-sensitive trace elements, such as V, Ni, Co, U, Cu, Cr, and Mn, exhibit strong enrichment under reducing conditions and hardly migrate during diagenesis (Kemp et al., 1994; Thomson et al., 1998; Pi et al., 2014; Lu et al., 2019; Tan et al., 2021), and are known as important redox indicators of ancient sedimentary water bodies (Dypvik, 1984; Powell et al., 2003; Li et al., 2016; Cheng et al., 2018; Liu et al., 2019a; Ali et al., 2022). Water stratification can be enhanced by highly saline water and S^{2-} which was brought by hydrothermal fluids (He et al., 2016; Wu et al., 2016). However, Ni/Co, Ni/V, (Cu + Mo)/Zn, U/Th and Uauth are of limited use in redox analysis of P^2l deposits (Jones and Manning, 1994; Pan et al., 2022). Zhang et al. (2018c) reported that the V/(V + Ni) ratios 0.46–0.60, 0.54–0.82, and >0.84 indicate dysoxic conditions, anoxic water with weak stratification, and euxinic water with strong stratification, respectively. The V/(V + Ni) ratios range from 0.33 to 0.82 (avg. 0.63) in Well FK-1, indicating the intermittent dysoxic-anoxic and weakly stratified water setting with frequent fluctuations, which confirmed the water setting noted by Pan et al. (2020) and Tao et al. (2022) in the Lucaogou Formation. In addition, the coexistence of framboid pyrite and horizontal bedding (Figures 3A, C) suggests a low-energy andeuxinic water setting that benefited organic matter preservation, and the significant correlation between Sr/Ba and Sr/Cu curves (Figure 7) suggest a good water sealing (Zhang et al., 2014) during deposition.

5.2.4 Water depth

Paleo-water depth are offen affected by sediment supply, climate changes, basin morphology, and tectonic settings (Carroll and Bohacs, 2001; Huuse and Clausen, 2001; Steinke et al., 2003; Annis et al., 2022), and can be estimated by sedimentological, lithological, biological and geochemical evidences (Immenhauser, 2001; Fritz et al., 2012; Rickard, 2019; Tessin et al., 2019; Tian et al., 2022). The abundant fine laminations in shale samples (Figures 2D, G, Figure 3A) suggest a low-energy depositional environment, whereas the wavy bedding and abundant dolomite (Figures 3D–F) present a shallower and agitated water, these are consistent with the starve profundal lake with periodic agitations described by Jiao et al. (2018). The ratio of (Al + Fe)/(Ca + Mg) have been utilized for demonstrating paleo-water depth, with higher ratios representing relatively deeper water (Liu et al., 2019a; Guan et al., 2021). The (Al+Fe)/(Ca+Mg) ratios in Well FK-1 range from 0.11 to 27.77 (avg. 1.54), indicating a fluctuated water depth during deposition (Figure 7). At a depth of 140–190 m, (Al + Fe)/(Ca + Mg) curve shows negative correlations with Sr/Ba, V/(V + Ni), and Sr/Cu curves, and can be divided into two parts: i) the rapidly increasing water depth (at a depth of 160–190 m) reduced the salinity and water stratification under a relatively humid climate; and ii) with the following prevalence of arid climate (at a depth of 140–160 m), the salinity and water stratification were reconstructed in the shallower water.

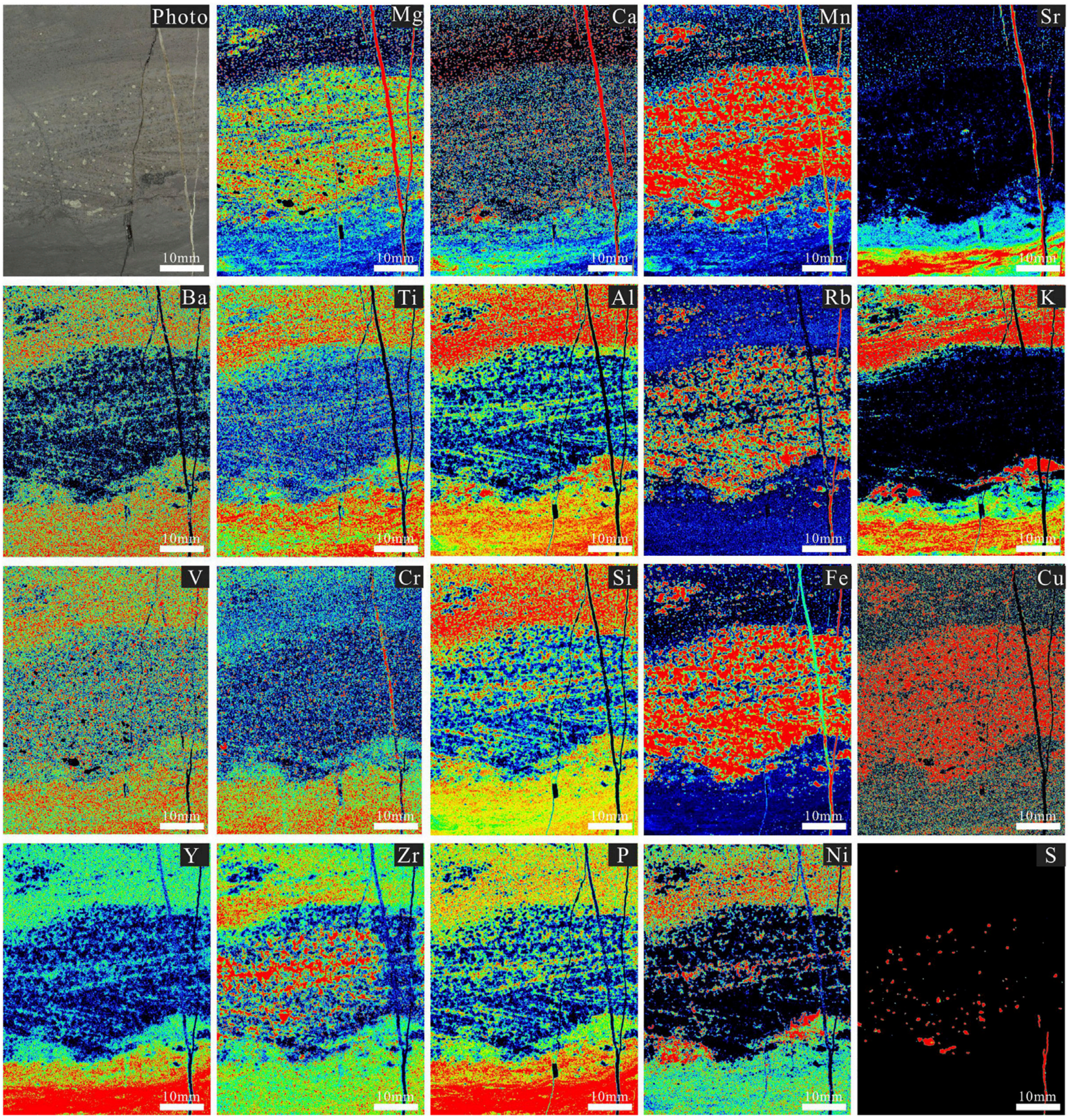

FIGURE 8
The μXRF elemental mapping of sample F1-18 (at a depth of 181.6 m) in Well FK-1, presenting divisional enrichments of Mg, Ca, Mn, Sr, Ba, Ti, Al, Rb, K, V, Cr, Si, Fe, Cu, Y, Zr, P, Ni, and S.

5.2.5 Productivity

Paleoproductivity, known as a prerequisite for the amount of organic matter produced in a certain geological period (Wei et al., 2020; Liu et al., 2021; Tan et al., 2021), can typically be evaluated using Ba, P, Cu, and TOC contents (Chen et al., 2020; Li et al., 2022). Ba usually precipitates in sediments with a high organic matter influx (Qiu et al., 2021) and shows correlations with high biomass productivity (Liu B. et al., 2015; Lu et al., 2019), whereas Al can describe the contribution of terrigenous input. Therefore the ratio of Ba/Al can demonstrate paleoproductivity and reveal similar variations with P/Al, and Cu/Al, the higher the ratio, the richer the productivity (Chen et al., 2016a; Qu et al., 2019; Pan et al., 2020). The Ba/Al ratios (0.002–0.06, avg. 0.01) in Well FK-1 demonstrate varied productivity during deposition, and the positive correlation between Ba/Al and (Fe + Mn)/Ti curves suggest that intermittent hydrothermal activities delivered nutrients into surface water and promoted the primary productivity, and eventually formed the organic-rich laminae (Liu et al., 2015a; Chen et al., 2016b; Zhang et al., 2019b; You et al., 2021; Li et al., 2022; Meng et al., 2022). Macerals including lamalginite, telaginite, and sporinite are abundant in shale samples in the Lucaogou Formation (Figures 3B, H; Xie et al., 2015; Liu et al., 2015a; Liu et al., 2017b; Pan et al., 2020; 2022), this is consistent with HI results in Well FK-1 (52–953 mg/g. TOC, avg. 410 mg/g. TOC) that the organic matter mainly belongs to oil-prone type and originated from terrestrial plants and algae during deposition (Hackley et al., 2016; Zhang et al., 2018c; Luo et al., 2018; Liu et al., 2022b; He et al., 2022). Detailed studies on biomarkers, including n-alkanes, regular steranes, and tricyclic terpanes suggest that

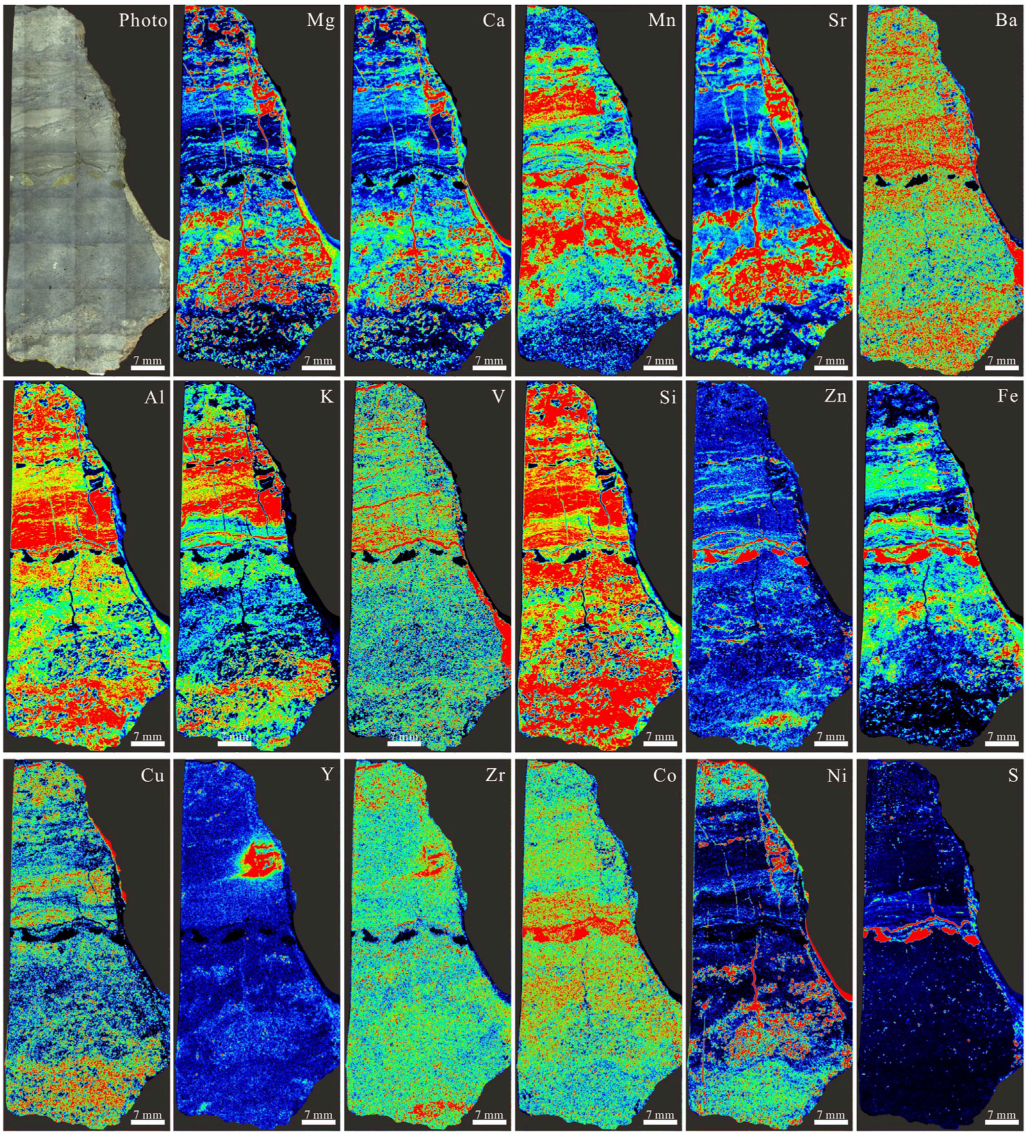

FIGURE 9
The µXRF elemental mapping of sample F1-78 (at a depth of 534.88 m) in Well FK-1, presenting divisional abundances of Mg, Ca, Mn, Sr, Ba, Al, K, V, Si, Zn, Fe, Cu, Y, Zr, Co, Ni, and S.

the dominant primary producers of organic matter in the Lucaogou Formation are algae and photosynthetic cyanobacteria (Cao et al., 2016; Liu et al., 2017a; Qu et al., 2017; Zhang et al., 2018b; Ding et al., 2019; Su et al., 2019). In addition, the TOC curve in Well FK-1 does not present a linear correlation with Ba/Al curve, because TOC is also controlled by preservation conditions in the Lucaogou Formation (Qiu et al., 2016b; Liu et al., 2019a; Qu et al., 2019; Jiang et al., 2020).

5.3 The mechanism of the organic matter enrichment during the early Permian

According to the above discussion, samples in Well FK-1 deposited during the Lucaogou Formation underwent intermittent hydrothermal events, of which five obvious episodes have been recognized. Hydrothermal activities exhibited significant effects on organic matter production and preservation during the Early Permian (Jiao et al., 2020; Meng et al., 2022), whereas TOC values in Well FK-1 did not show a simple linear correlation with hydrothermal intensities (Figure 7). Considering the rift-drift transition background of the basin (Peng, 2016; Wang et al., 2019a; Li et al., 2022), the uplift of the North Tianshan (Liu et al., 2018), and the lake transgression trend (Carroll, 1998; Liu et al., 2017b; Liu et al., 2022a), we proposed three patterns of organic matter enrichment that were strongly affected by intermittent hydrothermal events and paleoenvironmental changes in the southern Junggar Basin during the Early Permian (Figure 11).

(A) Low hydrothermal intensity and hot-arid climate in a rift basin with shallow water.

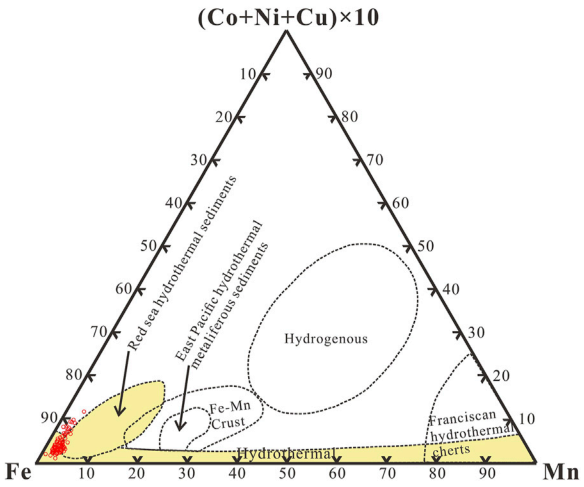

FIGURE 10
Ternary diagram of Fe vs. Mn vs. (Co + Ni + Cu) × 10 of shale samples in Well FK-1.

The first episode of hydrothermal events appeared at a depth of 495–545 m, with samples F1-78 (Figure 2I, Figure 9) and F1–79 (Figures 3D–F) as representatives. The second episode of hydrothermal events appeared at a depth of 415–475 m, with samples F1–63 (Figure 3I) and F1–64 (Figure 2F) as representatives. The hydrothermal intensities during these episodes were low; in the former episode, the (Fe+Mn)/Ti ratios range from 6.91 to 18.42 (avg. 11.05), whereas in the latter episode they range from 6.36 to 66.57 (avg. 16.24). The presence of monazite particles, fibrous mordenite (Figure 2I), and Y enrichment (Figure 9) indicate a near-magma-chamber eruption (Jiao et al., 2018), which coincide with the rift basin background during this time. In addition, the medium Sr/Ba, low (Al+Fe)/(Ca+Mg), and high Sr/Cu values (Figure 7), and the abundant dolomite with wavy bedding in sample F1–79 (Figure 2D), demonstrating that the water was saline and shallow under a hot-arid climate. With increasing hydrothermal intensity, the water column became less stratified and more oxidative, as represented by the decreasing V/(V+Ni) values, which could be a result of enhanced water circulation by underwater hydrothermal intrusion in an unstable rift basin. Therefore, the enhanced water circulation and hydrothermal diffusion not only delivered nutrients (e.g., Ba, Figure 6) into surface water and promoted algal blooming (Figure 3E), but also transported enough Ca^{2+}, Mg^{2+} ions (Figure 5) and precipitated abundant dolomite (Figures 3D, E) under a semi-arid climate.

In these two episodes, owing to the enhanced water circulation, which partially resulted from basin extension, nutrients carried by hydrothermal fluids were easily delivered into surface water and triggered primary productivity. However, from another perspective, the enhanced water circulation in the unstable basin destroyed the anoxic and well-stratified water conditions, resulting in more degradation and less preservation of organic matter. Therefore, the samples collected during these episodes did not own high TOC values.

(B) Medium-high hydrothermal intensity and a strongly hot-arid climate in a sub-stable basin with semi-deep water.

The third episode of hydrothermal events appeared at a depth of 270–400 m, with samples F1–33 (Figure 3H), F1–36 (Figures 2G, H) and F1–39 (Figure 2E) as representatives. The (Fe+Mn)/Ti values in this episode range from 5.32 to 119.72 (avg. 16.71), revealing a strong and upwardly increasing hydrothermal intensity. During this interval, strong hydrothermal fluids, with (Fe + Mn)/Ti values up to 68.31, damaged the former mud pebbles (Figure 2G) and precipitated specific hydrothermal minerals, including ZnS and zircon (Figures 2E, H). The fifth episode of hydrothermal events appeared at a depth of 40–70 m, with samples F1–2 (Figure 3G) and F1–6 (Figure 2D) as representatives. The (Fe+Mn)/Ti values in this episode range from 6.37 to 90.35 (avg. 26.06), and the tuff laminae and burrows filled with dolomite in F1–6 (Figure 2D) reveal intense hydrothermal precipitation in semi-deep water. The positive correlations between Ba/Al and (Fe + Mn)/Ti indicate that hydrothermal fluids delivered nutrients into surface water and excessively promoted primary productivity. In addition, in the third episode, the V/(V+Ni) values range from 0.50 to 0.75 (avg. 0.58–0.70), which reveal not only anoxic weak-stratified water but also successively decreasing trends in the intervals of 295–345 m and 385–400 m and increasing trends in the intervals of 270–295 m and 345–385 m (Figure 7), indicating a fluctuating water stratification in the sub-stable basin because of the rift-drift transition. Considering the consistent trends of the Sr/Ba, Sr/Cu, and (Fe + Mn)/Ti curves, the upward increase in hydrothermal intensity enhanced the salinity and aridity of the sub-stable basin. The increased amount of S^{2-} carried by hydrothermal fluids (demonstrated by the precipitation of ZnS and pyrite in Figure 2E) helped to reconstruct the anoxic and well-stratified conditions, which finally facilitated organic matter preservation and resulted in medium-high TOC values.

(C) Medium hydrothermal intensity and a humid climate in a stable basin with deep water

The fourth episode of hydrothermal events appeared at a depth of 135–255 m, with samples F1–10 (Figures 3A–C) and F1–18 (Figures 2A–C, Figure 8) as representatives. The (Fe+Mn)/Ti values in this episode range from 5.62 to 38.76 (avg. 12.07). Hydrothermal fluids, which are recorded as cross-bedding (Figure 2A), not only boiled the bottom water and left bubble-like aggregates of ankerite (Figures 2A, B), but also brought elements including Cu, Fe, Mn, S, and Zr (Figure 8) into the water column, helping to add nourishment to the surface water and construct an anoxic bottom water setting. The similarity of the (Fe + Mn)/Ti and Ba/Al curves and the enrichment of Ba and Cu (Figure 6) support the positive effect of hydrothermal intensity on promoting organic matter productivity.

In addition, (Al + Fe)/(Ca + Mg) ratios present a massive increase in the middle part of the fourth episode (at a depth of 165–215 m), whereas the V/(V + Ni) and Sr/Ba ratios experience the same strong negative excursion (Figure 7). Considering the low hydrothermal intensity during this time, the decrease in salinity, reducing conditions, and stratification of water can be attributed to

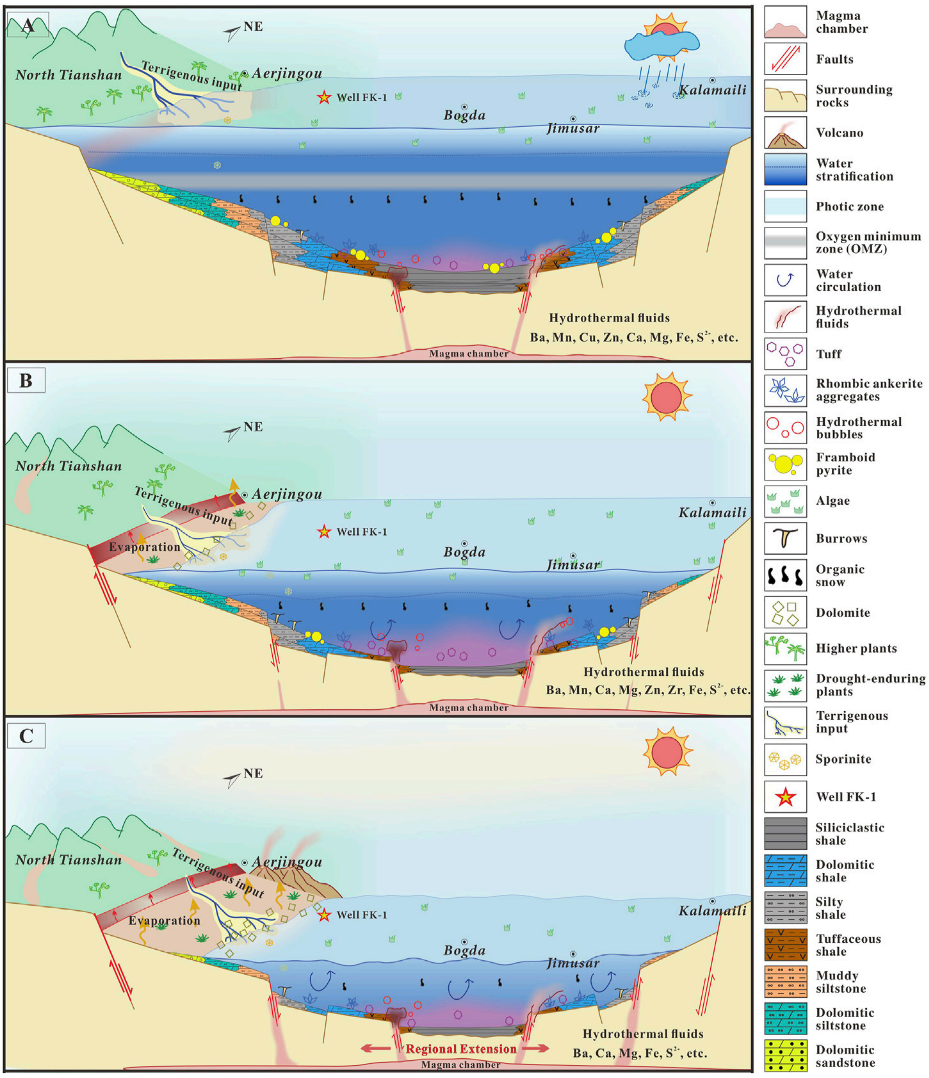

FIGURE 11
Three patterns of organic matter enrichment of the Early Permian Lucaogou Formation in Fukang Sag, southern Junggar Basin, NW China, indicating distinguishing leading roles of organic matter productivity and preservation during deposition. Pattern **(A)** presented low hydrothermal intensity and hot-arid climate in a rift basin with shallow water, pattern **(B)** owned the medium-high hydrothermal intensity and a strongly hot-arid climate in a sub-stable basin with semi-deep water, and pattern **(C)** exhibited medium hydrothermal intensity and a humid climate in a stable basin with deep water. Because of the low productivity and preservation, pattern **(A)** did not result in high organic matter enrichment, whereas patterns **(B)** and **(C)** presented better organic matter productivity and preservation, which resulted in medium-high TOC values.

the rapidly increasing water depth. This is consistent with the more humid climate and the deeper freshwater lake in the late sedimentation of the Lucaogou Formation (Carroll, 1998; Liu et al., 2022a). During this time, the humid climate and hydrothermal activities enhanced primary productivity, whereas the reduced salinity, reducing conditions, and stratification together impeded organic matter preservation, resulting in low-medium TOC values. In the 135–165 m interval, the V/(V + Ni) and Sr/Ba values rebounded under a hotter climate, and the enhanced salinity, reducing conditions and stratification of water were conducive for much better organic matter preservation (confirmed by abundant framboid pyrite in Figure 3C) and finally resulted in high TOC values. That is to say, even though the productivity was enhanced by the hydrothermal inputs and warm-humid climate, the preservation of organic matter played a leading role during this interval.

Patterns (A), (B), and (C) therefore demonstrate distinguishing leading roles in organic matter productivity and preservation in the Early Permian. During the rift-drift transition of the southern Junggar Basin, i) organic matter productivity fluctuated periodically, and reached the higher level in the third and fourth episodes because of the higher hydrothermal intensity and more warm-humid climate; whereas ii) preservation exhibited a trend of gradual increase with the paleoenvironmental changes in a relatively stable basin over time. Compared to pattern (B), pattern (C) presented better preservation because of the well-stratified deep water setting in a gradually stabilized basin.

6 Conclusion

We performed mineralogy and geochemistry analyses on core samples in Well FK-1 in Fukang Sag, southern Junggar Basin. The results revealed episodic hydrothermal events and paleoenvironmental changes that recorded in the Lucaogou Formation, and presented their impacts on the organic matter enrichment during deposition. The major research conclusions are as follows.

1) The high (Fe + Mn)/Ti ratios, the enrichment of Ca, Mg, Fe, Mn, and REY, and multiple hydrothermal minerals (e.g., ankerite, dolomite, zeolite, albite, and microcline) suggest episodic hydrothermal events in an Early Permian sedimentary succession in the southern Junggar Basin.
2) The varied Sr/Ba, V/(V + Ni), (Al + Fe)/(Ca + Mg), and Sr/Cu values indicate that the samples deposited in a brackish-saline, suboxic-anoxic, shallow to deep water setting under a warm-humid to hot-arid climate, with rhythmic flucutations.
3) The varied TOC content (up to 12.16 wt%), Ba/Al and HI values (up to 953 mg/g. TOC) reveal periodic organic matter enrichment in the Lucaogou Formation.
4) During the rift-drift transition of the southern Junggar Basin, three patterns of organic matter enrichment occurred. From patterns (A) to (C), productivity, which was triggered by warm-humid climate and nutrients delivered by hydrothermal events, fluctuated periodically; preservation was enhanced by saline, anoxic, well-stratified water under a hot-arid climate in a relatively stable basin, became progressively favorable over time and contributed to high TOC values.

Data availability statement

The original contributions presented in the study are included in the article/Supplementary Material, further inquiries can be directed to the corresponding author.

Author contributions

YJ, conceptualization, formal analysis, writing-original draft, methodology. CW, conceptualization, methodology, formal analysis, visualization, supervision, funding acquisition. TZ, Methodology, investigation, data curation. JW, Conceptualization, writing—original draft, visualization.

Funding

This work was supported by the National Natural Science Foundation of China (Grant No. 42072125).

Acknowledgments

The authors thank Yizhe Wang, Yanxi Zhou, and Jian Ma for performing the field work and sampling in the southern Junggar Basin. We are also indebted to Zhenhua Jing and Yuntao Ye for their assistance with pretreatment and measurement of samples. We are grateful to Yan Zhu and Nan Li for supporting the geochemistry analyses.

Conflict of interest

Author TZ was employed by the company PetroChina.

The remaining authors declare that the research was conducted in the absence of any commercial or financial relationships that could be construed as a potential conflict of interest.

Publisher's note

Supplementary material

The Supplementary Material for this article can be found online at: https://www.frontiersin.org/articles/10.3389/feart.2023.1182646/full#supplementary-material

References

Abdullahi, T., Harun, Z., and Othman, M. H. D. (2017). A review on sustainable synthesis of zeolite from kaolinite resources via hydrothermal process. *Adv. Powder. Technol.* 28, 1827–1840. doi:10.1016/j.apt.2017.04.028

Ali, F., Zhang, S. Q., Hanif, M., Mohibullah, M., Zhang, Y. X., Usman, M., et al. (2022). Geochemical investigation of low latitude black shale intervals of the Lower to Middle Jurassic succession, Indus Basin, Pakistan. *Front. Earth Sci-PRC.* 1-19, 568–586. doi:10.1007/s11707-021-0943-4

Annis, A., Karpack, M., Morrison, R. R., and Nardi, F. (2022). On the influence of river basin morphology and climate on hydrogeomorphic floodplain delineations. *Adv. Water Resour.* 159, 104078. doi:10.1016/j.advwatres.2021.104078

Baturin, G. N. (2012). Geochemistry of hydrothermal ferromanganese crusts of the Sea of Japan. *Dokl. Earth Sci.* 445 (1), 862. doi:10.1134/S1028334X12070112

Bonatti, E. (1975). Metallogenesis at oceanic spreading centers. *Annu. Rev. Earth. Pl. Sc.* 3, 401–431. doi:10.1146/annurev.ea.03.050175.002153

Brockamp, O., and Clauer, N. (2013). Hydrothermal and unexpected diagenetic alteration in Permian shales of the Lodève epigenetic U-deposit of southern France, traced by K-Ar illite and K-feldspar dating. *Chem. Geol.* 357, 18–28. doi:10.1016/j.chemgeo.2013.08.009

Cao, Z., Liu, G. D., Kong, Y. H., Wang, C. Y., Niu, Z. C., Zhang, J. Y., et al. (2016). Lacustrine tight oil accumulation characteristics: Permian Lucaogou Formation in jimusaer sag, Junggar Basin. *Int. J. Coal. Geol.* 153, 37–51. doi:10.1016/j.coal.2015.11.004

Carroll, A. R., and Bohacs, K. M. (2001). Lake-type controls on petroleum source rock potential in nonmarine basins. *AAPG Bull.* 85 (6), 1033–1053.

Carroll, A. R., Brassell, S. C., and Graham, S. A. (1992). Upper permian lacustrine oil shales, southern Junggar Basin, northwest China. *AAPG Bull.* 76 (12), 1874–1902.

Carroll, A. R. (1998). Upper Permian lacustrine organic facies evolution, southern Junggar Basin, NW China. *Org. Geochem.* 28 (11), 649–667. doi:10.1016/s0146-6380(98)00040-0

Chao, E. C. T., Black, J. M., Minkin, J. A., Tatsumoto, M., Wang, J. W., Conrad, J. E., et al. (1997). The sedimentary carbonate-hosted giant bayan obo REE-Fe-Nb ore deposit of inner Mongolia, China: A cornerstone example for giant polymetallic ore deposits of hydrothermal origin. *U.S. Geol. Surv. Bull.* 2143.

Chen, C., Mu, C. L., Zhou, K. K., Liang, W., Ge, X. Y., Wang, X. P., et al. (2016a). The geochemical characteristics and factors controlling the organic matter accumulation of the Late Ordovician-Early Silurian black shale in the Upper Yangtze Basin, South China. *Mar. Pet. Geol.* 76, 159–175. doi:10.1016/j.marpetgeo.2016.04.022

Chen, G., Gang, W. Z., Chang, X. C., Wang, N., Zhang, P. F., Cao, Q. Y., et al. (2020). Paleoproductivity of the chang 7 unit in the ordos basin (north China) and its controlling factors. *Palaeogeogr. Palaeoclimatol. Palaeoecol.* 551, 109741. doi:10.1016/j.palaeo.2020.109741

Chen, J. Q., Pang, X. Q., Pang, H., Chen, Z. H., and Jiang, C. Q. (2018). Hydrocarbon evaporative loss evaluation of lacustrine shale oil based on mass balance method: Permian Lucaogou Formation in Jimusaer Depression, Junggar Basin. *Mar. Pet. Geol.* 91, 422–431. doi:10.1016/j.marpetgeo.2018.01.021

Chen, Z. H., Huang, W., Liu, Q., Zhang, L. Y., and Zhang, S. C. (2016b). Geochemical characteristics of the paleogene shales in the dongying depression, eastern China. *Mar. Pet. Geol.* 73, 249–270. doi:10.1016/j.marpetgeo.2016.02.022

Cheng, B., Xu, J. B., Liang, Y. G., Deng, Q., Tian, Y. K., and Liao, Z. W. (2018). Determination and geochemical implication of multiple series of long-chain oxygen-bearing compounds trapped in kerogen in the Lucaogou Formation, Santanghu Basin, NW China. *Org. Geochem.* 121, 68–79. doi:10.1016/j.orggeochem.2018.04.005

Cheng, D. W., Zhou, C. M., Zhang, Z. J., Yuan, X. J., Liu, X. J., and Chen, X. Y. (2022). Paleo-environment reconstruction of the middle permian Lucaogou Formation, southeastern Junggar Basin, NW China: Implications for the mechanism of organic matter enrichment in ancient lake. *J. Earth. Sci-China* 33, 963–976. doi:10.1007/s12583-020-1073-8

Cheng, M., Li, C., Jin, C. S., Wang, H. Y., Algeo, T. J., Lyons, T. W., et al. (2020). Evidence for high organic carbon export to the early Cambrian seafloor. *Geochim. Cosmochim. Ac* 287, 125–140. doi:10.1016/j.gca.2020.01.050

Dai, S. F., Graham, I. T., and Ward, C. R. (2016). A review of anomalous rare Earth elements and yttrium in coal. *Int. J. Coal. Geol.* 159, 82–95. doi:10.1016/j.coal.2016.04.005

Dang, B., Zhao, H., Chen, J., Zheng, Y., Xu, M., Lin, L. J., et al. (2019). Accumulation condition analysis of the permian shale gas in the Turpan-Hami Basin, northwest China. *Geol. J.* 54, 4051–4065. doi:10.1002/gj.3486

Ding, X. J., Qu, J. X., Imin, A., Zha, M., Su, Y., Jiang, Z. F., et al. (2019). Organic matter origin and accumulation in tuffaceous shale of the lower Permian Lucaogou Formation, Jimsar Sag. *J. Pet. Sci. Eng.* 179, 696–706. doi:10.1016/j.petrol.2019.05.004

Douville, E., Bienvenu, P., Charlou, J., Donval, J. P., Fouquet, Y., Appriou, P., et al. (1999). Yttrium and rare Earth elements in fluids from various deep-sea hydrothermal systems. *Geochim. Cosmochim. Ac* 63 (5), 627–643. doi:10.1016/s0016-7037(99)00024-1

Dypvik, H. (1984). Geochemical compositions and depositional conditions of upper jurassic and lower cretaceous yorkshire clays, england. *Geol. Mag.* 121 (5), 489–504. doi:10.1017/s0016756800030028

Farrimond, P., Eglinton, G., Brassell, S. C., and Jenkyns, H. C. (1989). Toarcian anoxic event in Europe: An organic geochemical study. *Mar. Pet. Geol.* 6 (2), 136–147. doi:10.1016/0264-8172(89)90017-2

Flude, S., Haschke, M., and Storey, M. (2017). Application of benchtop micro-XRF to geological materials. *Mineral. Mag.* 81 (4), 923–948. doi:10.1180/minmag.2016.080.150

Frisia, S., Borsato, A., Drysdale, R. N., Paul, B., Greig, A., and Cotte, M. (2012). A re-evaluation of the palaeoclimatic significance of phosphorus variability in speleothems revealed by high-resolution synchrotron micro XRF mapping. *Clim. Past.* 8 (6), 2039–2051. doi:10.5194/cp-8-2039-2012

Fritz, S. C., Baker, P. A., Tapia, P., Spanbauer, T., and Westover, K. (2012). Evolution of the Lake Titicaca basin and its diatom flora over the last ~370,000 years. *Palaeogeogr. Palaeoclimatol. Palaeoecol.* 317-318, 93–103. doi:10.1016/j.palaeo.2011.12.013

Gao, P., He, Z. L., Li, S. J., Lash, G. G., Li, B. Y., Huang, B. Y., et al. (2018). Volcanic and hydrothermal activities recorded in phosphate nodules from the lower Cambrian Niutitang Formation black shales in South China. *Palaeogeogr. Palaeoclimatol. Palaeoecol.* 505, 381–397. doi:10.1016/j.palaeo.2018.06.019

Gao, Y., Huang, H., Tao, H. F., Carroll, A. R., Qin, J. M., Chen, J. Q., et al. (2020). Paleoenvironmental setting, mechanism and consequence of massive organic carbon burial in the Permian Junggar Basin, NW China. *J. Asian. Earth. Sci.* 194, 104222. doi:10.1016/j.jseaes.2019.104222

Gao, Y., Wang, Y. L., Peng, P. A., He, D. X., Wang, G., Wang, Z. X., et al. (2016). Source rock potential and depositional environment of upper Permian oil shales of the Lucaogou formation in the southern Junggar Basin, Northwest China. *Oil Shale* 33 (4), 299–328. doi:10.3176/oil.2016.4.01

German, C. R., Baker, E. T., Connelly, D. P., Lupton, J. E., Resing, J., Prien, R. D., et al. (2006). Hydrothermal explorations of the fonualei rift and spreading center and the northeast lau spreading center. *Geochem. Geophys. Geosystems* 7 (11), 1–15. doi:10.1029/2006GC001324

Guan, M. D., Wu, S. T., Hou, L. H., Jiang, X. H., Ba, D., and Hua, G. L. (2021). Paleoenvironment and chemostratigraphy heterogenity of the Cretaceous organic-rich shales. *Adv. Geo-Energy Res.* 5 (4), 444–455. doi:10.46690/ager.2021.04.09

Hackley, P. C., Fishman, N., Wu, T., and Baugher, G. (2016). Organic petrology and geochemistry of mudrocks from the lacustrine Lucaogou Formation, Santanghu Basin, northwest China: Application to lake basin evolution. *Int. J. Coal. Geol.* 168, 20–34. doi:10.1016/j.coal.2016.05.011

Hadad, Y. T., Hakimi, H. M., Abdulla, W. H., Kinawy, M., Mahdy, O. E., and Lashin, A. (2021). Organic geochemical characteristics of Zeit source rock from Red Sea Basin and their contribution to organic matter enrichment and hydrocarbon generation potential. *J. Afr. Earth. Sci.* 177, 104151. doi:10.1016/j.jafrearsci.2021.104151

Han, C. L., Cai, W. P., Tang, W., Wang, G. Z., and Liang, C. H. (2011). Protein assisted hydrothermal synthesis of ultrafine magnetite nanoparticle built-porous oriented fibers and their structurally enhanced adsorption to toxic chemicals in solution. *J. Marter. Chem.* 21 (30), 11188–11196. doi:10.1039/c1jm11048a

Haskin, L. A., Frey, F. A., Schimitt, R. A., and Smith, R. H. (1966). Meteoritic, solar and terrestrial rare-Earth distributions. *Physisc Chem. Earth* 7, 167–321. doi:10.1016/0079-1946(66)90004-8

He, C., Ji, L. M., Wu, Y. D., Su, A., and Zhang, M. Z. (2016). Characteristics of hydrothermal sedimentation process in the Yanchang Formation, south Ordos Basin, China: Evidence from element geochemistry. *Sediment. Geol.* 345, 33–41. doi:10.1016/j.sedgeo.2016.09.001

He, T. H., Lu, S. F., Li, W. H., Tan, Z. Z., and Zhang, X. W. (2018). Effect of salinity on source rock formation and its control on the oil content in shales in the Hetaoyuan Formation from the Biyang Depression, Nanxiang Basin, Central China. *Energy Fuel.* 32, 6698–6707. doi:10.1021/acs.energyfuels.8b01075

He, W. J., Liu, Y., Wang, D. X., Lei, D. W., Liu, G. D., Gao, G., et al. (2022). Geochemical characteristics and process of hydrocarbon generation evolution of the Lucaogou Formation shale, jimsar depression, Junggar Basin. *Energies* 15, 2331. doi:10.3390/en15072331

Hosterman, J. W., and Whitlow, S. I. (1981). Munsell color value as related to organic carbon in devonian shale of appalachian basin. *AAPG Bull.* 65 (2), 333–335.

Hu, T., Pang, X. Q., Jiang, S., Wang, Q. F., Xu, T. W., Lu, K., et al. (2018). Impact of paleosalinity, dilution, redox, and paleoproductivity on organic matter enrichment in a saline lacustrine rift basin: A case study of paleogene organic-rich shale in dongpu depression, bohai bay basin, eastern China. *Energy Fuel* 32 (4), 5045–5061. doi:10.1021/acs.energyfuels.8b00643

Hu, T., Pang, X. Q., Wang, Q. F., Jiang, S., Wang, X. L., Huang, C., et al. (2017). Geochemical and geological characteristics of permian Lucaogou Formation shale of the well Ji174, jimusar sag, Junggar Basin, China: Implications for shale oil exploration. *Geol. J.* 53 (5), 2371–2385. doi:10.1002/gj.3073

Huang, X. W., Sappin, A., Boutroy, E., Beaudoin, G., and Makvandi, S. (2019). Trace element composition of igneous and hydrothermal magnetite from porphyry deposits: Relationship to deposit subtypes and magmatic affinity. *Econ. Geol.* 114 (5), 917–952. doi:10.5382/econgeo.4648

Huuse, M., and Clausen, O. R. (2001). Morphology and origin of major cenozoic sequence boundaries in the eastern north sea basin: Top eocene, near-top oligocene and the mid-miocene unconformity: Major cenozoic sequence boundaries, E north sea. *Basin. Res.* 13 (1), 17–41. doi:10.1046/j.1365-2117.2001.00123.x

Immenhauser, A. (2001). Estimating palaeo-water depth from the physical rock record. *Earth-Sci. Rev.* 96 (1-2), 107–139. doi:10.1016/j.earscirev.2009.06.003

Incerpi, N., Manatschal, G., Martire, L., Bernasconi, S. M., Gerdes, A., and Bertok, C. (2020). Characteristics and timing of hydrothermal fluid circulation in the fossil pyrenean hyperextended rift system: New constraints from the chainons bearnais (W pyrenees). *Int. J. Earth. Sci.* 109 (3), 1071–1093. doi:10.1007/s00531-020-01852-6

Jia, J. L., Bechtel, A., Liu, Z. J., Strobl, S. A. I., Sun, P. C., and Sachsenhofer, R. F. (2013). Oil shale Formation in the upper cretaceous nenjiang Formation of the songliao basin (NE China): Implications from organic and inorganic geochemical analyses. *Int. J. Coal. Geol.* 113, 11–26. doi:10.1016/j.coal.2013.03.004

Jiang, Y. H., Hou, D. J., Li, H., Zhang, Z. M., and Guo, R. B. (2020). Impact of the paleoclimate, paleoenvironment, and algae bloom: Organic matter accumulation in the lacustrine Lucaogou Formation of jimsar sag, Junggar Basin, NW China. *Energies* 13 (6), 1488–1510. doi:10.3390/en13061488

Jiang, Y. Q., Liu, Y. Q., Yang, Z., Nan, Y., Wang, R., Zhou, P., et al. (2015). Characteristics and origin of tuff-type tight oil in Jimusaer sag, Junggar Basin, NW China. *Pet. explor. Dev+* 42 (6), 810–818. doi:10.1016/s1876-3804(15)30077-x

Jiao, J. G., Han, F., Zhao, L. D., Duan, J., and Wang, M. X. (2019). Magnetite geochemistry of the jinchuan Ni-Cu-pge deposit, NW China: Implication for its ore-forming processes. *Minerals* 9, 593. doi:10.3390/min9100593

Jiao, X., Liu, Y. Q., Yang, W., Zhou, D. W., Bai, B., Zhang, T. S., et al. (2020). Fine-grained volcanic-hydrothermal sedimentary rocks in Permian Lucaogou Formation, Santanghu Basin, NW China: Implications on hydrocarbon source rocks and accumulation in lacustrine rift basins. *Mar. Pet. Geol.* 114, 104201. doi:10.1016/j.marpetgeo.2019.104201

Jiao, X., Liu, Y. Q., Yang, W., Zhou, D. W., Li, H., Nan, Y., et al. (2018). A magmatic-hydrothermal lacustrine exhalite from the Permian Lucaogou Formation, Santanghu Basin, NW China - the volcanogenic origin of fine-grained clastic sedimentary rocks. *J. Asian. Earth. Sci.* 156, 11–25. doi:10.1016/j.jseaes.2018.01.011

Jones, B., and Manning, D. A. C. (1994). Comparison of geochemical indices used for the interpretation of palaeoredox conditions in ancient mudstones. *Chem. Geol.* 111 (1-4), 111–129. doi:10.1016/0009-2541(94)90085-x

Kadar, E., Costa, V., and Santos, R. S. (2006). Distribution of micro-essential (Fe, Cu, Zn) and toxic (Hg) metals in tissues of two nutritionally distinct hydrothermal shrimps. *Sci. Total Environ.* 358 (1-3), 143–150. doi:10.1016/j.scitotenv.2005.09.003

Kemp, A. J., Palmer, M. R., and Ragnarsdottir, K. V. (1994). The Uranium-Thorium and rare Earth element geochemistry of reduction nodules from Budleigh Salterton, Devon. *Read A. T. Annu. Conf. Ussher Soc.* 8, 214.

Kim, J. J., Ling, F. T., Plattenberger, D. A., Clarens, A. F., Lanzirotti, A., Newville, M., et al. (2021). SMART mineral mapping: Synchrotron-based machine learning approach for 2D characterization with coupled micro XRF-XRD. *Comput. Geosci-UK.* 156, 104898. doi:10.1016/j.cageo.2021.104898

Li, B. Q., Zhuang, X. G., Liu, X. F., Wu, C., Zhou, J. B., and Ma, X. P. (2016). Mineralogical and geochemical composition of middle permian Lucaogou formatiodfn in the southern Junggar Basin, China: Implications for paleoenvironment, provenance, and tectonic setting. *Arab. J. Geosci.* 9 (3), 1–16. doi:10.1007/s12517-015-2154-3

Li, D. L., Li, R. X., Zhu, Z. W., Wu, X. L., Liu, F. T., Zhao, B. S., et al. (2018). Influence on lacustrine source rock by hydrothermal fluid: A case study of the chang 7 oil shale, southern ordos basin. *Acta Geochim.* 37, 215–227. doi:10.1007/s11631-017-0203-1

Li, H., Liu, Y. Q., Yang, K., Liu, Y. J., and Niu, Y. Z. (2021a). Hydrothermal mineral assemblages of calcite and dolomite-analcime-pyrite in Permian lacustrine Lucaogou mudstones, eastern Junggar Basin, Northwest China. *Mineralogy Petrology* 115, 63–85. doi:10.1007/s00710-020-00726-8

Li, J. H., Pei, R., Teng, F. F., Qiu, H., Tagle, R., Yan, Q. Q., et al. (2021b). Micro-XRF study of the troodontid dinosaur Jianianhualong tengi reveals new biological and taphonomical signals. *BioRxiv* 41, 1–11. doi:10.46770/as.2021.01.001

Li, Q., Liu, G. D., Song, Z. Z., Zhang, B. J., Sun, M. L., Tian, X. W., et al. (2022). Organic matter enrichment due to high primary productivity in the deep-water shelf: Insights from the lower Cambrian Qiongzhusi shales of the central Sichuan Basin, SW China. *J. Asian. Earth. Sci.* 239, 105417. doi:10.1016/j.jseaes.2022.105417

Li, T. J., Huang, Z. L., Yin, Y., Gou, H. G., and Zhang, P. (2020a). Sedimentology and geochemistry of Cretaceous source rocks from the Tiancao Sag, Yin'e Basin, North China: Implications for the enrichment mechanism of organic matters in small lacustrine rift basins. *J. Asian. Earth. Sci.* 204, 104575. doi:10.1016/j.jseaes.2020.104575

Li, Y. F., Zhang, T. W., Ellis, G. S., and Shao, D. Y. (2017a). Depositional environment and organic matter accumulation of upper ordovician–lower silurian marine shale in the upper yangtze platform, south China. *Palaeogeogr. Palaeoclimatol. Palaeoecol.* 466, 252–264. doi:10.1016/j.palaeo.2016.11.037

Li, Y. J., Sun, P. C., Liu, Z. J., Wang, J. X., Li, Y., and Zhang, M. Q. (2019). Lake level controls on oil shale distribution in the Lucaogou Formation, wujiawan area, Junggar Basin, northwest China. *Energy fuels.* 33 (9), 8383–8393. doi:10.1021/acs.energyfuels.9b01884

Li, Y. J., Sun, P. C., Liu, Z. J., Yao, S. Q., Xu, Y. B., Liu, R., et al. (2020b). Geochemistry of the permian oil shale in the northern Bogda mountain, Junggar Basin, northwest China: Implications for weathering, provenance and tectonic setting. *ACS Earth. Space. Chem.* 4 (8), 1332–1348. doi:10.1021/acsearthspacechem.0c00113

Li, Z. X., Liu, Y. Q., Jiao, X., and Li, H. (2017b). The characteristics of the hydrothermal exhalative dolostone of Lucaogou Formation in Santanghu basin and its geology setting indication. *Acta Geol. Sin.* 91 (1), 131. doi:10.1111/1755-6724.13221

Liang, J. L., Tang, D. Z., Xu, H., Tao, S., Li, C. C., and Gou, M. (2014). Formation conditions of Jimusaer oil shale at the northern foot of Bogda Mountain, China. *Oil Shale* 31 (1), 19–29. doi:10.3176/oil.2014.1.03

Lima, B. E. M., and De Ros, L. F. (2019). Deposition, diagenetic and hydrothermal processes in the Aptian Pre-Salt lacustrine carbonate reservoirs of the northern Campos Basin, offshore Brazil. *Sediment. Geol.* 383, 55–81. doi:10.1016/j.sedgeo.2019.01.006

Lin, M. R., Xi, K. L., Cao, Y. C., Liu, Q. Y., Zhang, Z. H., and Li, K. (2021). Petrographic features and diagenetic alteration in the shale strata of the permian Lucaogou Formation, jimusar sag, Junggar Basin. *J. Pet. Sci. Eng.* 203, 108684. doi:10.1016/j.petrol.2021.108684

Liu, B., Bechtel, A., Sachsenhofer, R. F., Gross, D., Gratzer, R., and Chen, X. (2017a). Depositional environment of oil shale within the second member of permian Lucaogou Formation in the Santanghu Basin, northwest China. *Int. J. Coal. Geol.* 175, 10–25. doi:10.1016/j.coal.2017.03.011

Liu, B., Lü, Y. F., Meng, Y. L., Li, X. N., Guo, X. B., Ma, Q., et al. (2015a). Petrologic characteristics and genetic model of lacustrine lamellar fine-grained rock and its significance for shale oil exploration: A case study of permian Lucaogou Formation in malang sag, Santanghu Basin, NW China. *Pet. explor. Dev+* 42 (5), 656–666. doi:10.1016/s1876-3804(15)30060-4

Liu, B., Song, Y., Zhu, K., Su, P., Ye, X., and Zhao, W. C. (2020). Mineralogy and element geochemistry of salinized lacustrine organic-rich shale in the Middle Permian Santanghu Basin: Implications for paleoenvironment, provenance, tectonic setting and shale oil potential. *Mar. Pet. Geol.* 120, 104569. doi:10.1016/j.marpetgeo.2020.104569

Liu, C., Liu, K. Y., Wang, X. Q., Wu, L. Y., and Fan, Y. C. (2019a). Chemostratigraphy and sedimentary facies analysis of the permian Lucaogou Formation in the jimusaer sag, Junggar Basin, NW China: Implications for tight oil exploration. *J. Asian. Earth. Sci.* 178, 96–111. doi:10.1016/j.jseaes.2018.04.013

Liu, C., Liu, K. Y., Wang, X. Q., Zhu, R. K., Wu, L. Y., and Xu, X. Y. (2019b). Chemo-sedimentary facies analysis of fine-grained sediment formations: An example from the Lucaogou Fm in the Jimusaer Sag, Junggar Basin, NW China. *Mar. Pet. Geol.* 110, 388–402. doi:10.1016/j.marpetgeo.2019.06.043

Liu, D. D., Fan, Q. Q., Zhang, C., Gao, Y., Du, W., Song, Y., et al. (2022a). Paleoenvironment evolution of the permian Lucaogou Formation in the southern Junggar Basin, NW China. *Palaeogeogr. Palaeoclimatol. Palaeoecol.* 603, 111198. doi:10.1016/j.palaeo.2022.111198

Liu, D. D., Kong, X. Y., Zhang, C., Wang, J. B., Yang, D. X., Liu, X. Y., et al. (2018). Provenance and geochemistry of lower to middle permian strata in the southern junggar and turpan basins: A terrestrial record from mid-latitude ne pangea. *Palaeogeogr. Palaeoclimatol. Palaeoecol.* 495, 259–277. doi:10.1016/j.palaeo.2018.01.020

Liu, S. J., Gao, G., Jun, J., Misch, D., Wu, X. S., Gang, W. Z., et al. (2022b). Mechanism of differential enrichment of shale oils in the upper and lower members of the Lucaogou Formation in the Jimusaer Sag, Junggar Basin. *Mar. Pet. Geol.* 142, 105747. doi:10.1016/j.marpetgeo.2022.105747

Liu, Y. M., Ma, K., Hou, J. G., Yan, L., and Chen, F,L. (2019d). Diagenetic controls on the quality of the middle permian Lucaogou Formation tight reservoir southeastern Junggar Basin, northwestern China. *J. Asian. Earth. Sci.* 178, 139–155. doi:10.1016/j.jseaes.2018.09.024

Liu, Y. Q., Jiao, X., Li, H., Yuan, M. S., Yang, W., Zhou, X. H., et al. (2012). Primary dolostone formation related to mantle-originated exhalative hydrothermal activities, Permian Yuejingou section, Santanghu area, Xinjiang, NW China. *Sci. China. Earth. Sci.* 55 (2), 183–192. doi:10.1007/s11430-011-4356-1

Liu, Z. H., Zhuang, X. G., Teng, G. E., Xie, X. M., Yin, L. M., Bian, L. Z., et al. (2015b). The Lower Cambrian Niutitang Formation at Yangtiao (Guizhou, SW China): Organic matter enrichment, source rock potential, and hydrothermal influences. *J. Pet. Geol.* 38 (4), 411–432. doi:10.1111/jpg.12619

Liu, Z. J., Meng, Q. T., Dong, Q. S., Zhu, J. W., Guo, W., Ye, S. Q., et al. (2017b). Characteristics and resource potential of oil shale in China. *Oil Shale* 34 (1), 15–41. doi:10.3176/oil.2017.1.02

Liu, Z. X., Yan, D. T., Du, X. B., and Li, S. J. (2021). Organic matter accumulation of the early Cambrian black shales on the flank of Micangshan-Hannan Uplift, northern upper Yangtze Block, South China. *J. Pet. Sci. Eng.* 200, 108378. doi:10.1016/j.petrol.2021.108378

Loukola-Ruskeeniemi, K., and Heino, T. (1996). Geochemistry and Genesis of the black shale-hosted Ni-Cu-Zn deposit at Talvivaara, Finland. *Finl. Econ. Geol.* 91 (1), 80–110. doi:10.2113/gsecongeo.91.1.80

Lu, Y. B., Jiang, S., Lu, Y. C., Xu, S., Shu, Y., and Wang, Y. X. (2019). Productivity or preservation? The factors controlling the organic matter accumulation in the late katian through hirnantian wufeng organic-rich shale, south China. *Mar. Pet. Geol.* 109, 22–35. doi:10.1016/j.marpetgeo.2019.06.007

Luo, Q. Y., Gong, L., Qu, Y. S., Zhang, K. H., Zhang, G. L., and Wang, S. Z. (2018). The tight oil potential of the Lucaogou Formation from the southern Junggar Basin, China. *Fuel* 234, 858–871. doi:10.1016/j.fuel.2018.07.002

Malisa, E. (2003). Trace elements characterization of the hydrothermally deposited tanzanite and green grossular in the Merelani-Lelatema shear zone, northeastern Tanzania. *Tanzan. J. Sci.* 29 (1), 45–60. doi:10.4314/tjs.v29i1.18366

Meng, Z. Y., Liu, Y. Q., Jiao, X., Ma, L. T., Zhou, D. W., Li, H., et al. (2022). Petrological and organic geochemical characteristics of the permian Lucaogou Formation in the jimsar sag, Junggar Basin, NW China: Implications on the relationship between hydrocarbon accumulation and volcanic-hydrothermal activities. *J. Pet. Sci. Eng.* 210, 110078. doi:10.1016/j.petrol.2021.110078

Meunier, J. D., Landais, P., monthioux, M., and Pagel, M. (1987). "Oxidation-reduction processes in the Genesis of the uranium-vanadium tabular deposits of the Cottonwood Wash mining area (Utah, U.S.A.): evidence from petrological study and organic matter analysis," in *Bulletin de Mineralogie*. Editor R. C. Willaime (USA: Masson).

Moore, L. R. (1969). "Geomicrobiology and geomicrobiological attact on sedimented organic matter," in *Organic geochemistry: Methods and results*. Editors G. Eglinton, and M. T. J. Murphy (Germany: Springer Science & Business Media), 265–303.

Mouro, L. D., Pacheco, M. L. A. F., Ricetti, J. H. Z., Scomazzon, A. K., Horodyski, R. S., Fernandes, A. C. S., et al. (2020). Lontras Shale (Paraná Basin, Brazil): Insightful analysis and commentaries on paleoenvironment and fossil preservation into a deglaciation pulse of the Late Paleozoic Ice Age. *Palaeogeogr. Palaeoclimatol. Palaeoecol.* 555, 109850. doi:10.1016/j.palaeo.2020.109850

Negrete-Aranda, R., Neumann, F., Contreras, J., Harries, R. N., Spelz, R. M., Zierenberg, R., et al. (2021). Transport of Heat by Hydrothermal Circulation in a Young Rift Setting: Observations From the Auka and JaichMaa Ja'ag' Vent Field in the Pescadero Basin, Southern Gulf of California. *J. Geophys. Res-Sol. Ea.* 126 (8), 1–20. doi:10.1029/2021jb022300

Noori, H., Mehrabi, H., Rahimpour-Bonab, H., and Faghih, A. (2019). Tectono-sedimentary controls on Lower Cretaceous carbonate platforms of the central Zagros, Iran: An example of rift-basin carbonate systems. *Mar. Pet. Geol.* 110, 91–111. doi:10.1016/j.marpetgeo.2019.07.008

Norin, E. (1955). The mineral composition of the Napolitan yellow tuff. *Geol. Rundsch.* 43 (2), 526–534. doi:10.1007/bf01764038

Orberger, B., Gallien, J.-P., Pinti, D. L., Fialin, M., Daudin, L., Gröcke, D. R., et al. (2005). Nitrogen and carbon partitioning in diagenetic and hydrothermal minerals from

Paleozoic Black Shales, (Selwyn Basin, Yukon Territories, Canada). *Chem. Geol.* 218 (3-4), 249–264. doi:10.1016/j.chemgeo.2005.01.012

Pan, Y. S., Huang, Z. L., Guo, X. B., Wang, R., Lash, G. G., Fan, T. G., et al. (2022). A re-assessment and calibration of redox thresholds in the Permian Lucaogou Formation of the Malang Sag, Santanghu Basin, Northwest China. *Mar. Pet. Geol.* 135, 105406. doi:10.1016/j.marpetgeo.2021.105406

Pan, Y. S., Huang, Z. L., Li, T. J., Guo, X. B., Xu, X. F., and Chen, X. (2020). Environmental response to volcanic activity and its effect on organic matter enrichment in the Permian Lucaogou Formation of the Malang Sag, Santanghu Basin, Northwest China. *Palaeogeogr. Palaeoclimatol. Palaeoecol.* 560, 110024. doi:10.1016/j.palaeo.2020.110024

Pang, H., Pang, X. Q., Dong, L., and Zhao, X. (2018). Factors impacting on oil retention in lacustrine shale: Permian Lucaogou Formation in Jimusaer Depression, Junggar Basin. *J. Pet. Sci. Eng.* 163, 79–90. doi:10.1016/j.petrol.2017.12.080

Payne, R. J., and Egan, J. (2019). Using palaeoecological techniques to understand the impacts of past volcanic eruptions. *Quatern. Int.* 499, 278–289. doi:10.1016/j.quaint.2017.12.019

Peng, X. W. (2016). “Provenance and depositional environments of fluvial-lacustrine sandstones of lower Permian Lucaogou low-order cycle, Bogda Mountains, NW China,” in *A thesis for master of science in Geology & Geophysics*. Editor X. W. Peng (China: Missouri University of Science and Technology ProQuest Dissertations Publishing).

Pi, D. H., Jiang, S. Y., Luo, L., Yang, J. H., and Ling, H. F. (2014). Depositional environments for stratiform witherite deposits in the Lower Cambrian black shale sequence of the Yangtze Platform, southern Qinling region, SW China: Evidence from redox-sensitive trace element geochemistry. *Palaeogeogr. Palaeoclimatol. Palaeoecol.* 398, 125–131. doi:10.1016/j.palaeo.2013.09.029

Potter, N., and Brand, N. (2019). Application of micro-XRF to characterise diamond drill-core from lithium-caesium-tantalum pegmatites. *ASEG Ext. Abstr.* 1, 1–4. doi:10.1080/22020586.2019.12073139

Powell, W. G., Johnston, P. A., and Collom, C. J. (2003). Geochemical evidence for oxygenated bottom waters during deposition of fossiliferous strata of the Burgess Shale Formation. *Palaeogeogr. Palaeoclimatol. Palaeoecol.* 201 (3-4), 249–268. doi:10.1016/s0031-0182(03)00612-6

Pratt, L. M. (1984). Influence of Paleoenvironmental Factors on Preservation of Organic Matter in Middle Cretaceous Greenhorn Formation, Pueblo, Colorado. *AAPG Bull.* 68 (9), 1146–1159.

Qiu, Z., Shi, Z. S., Dong, D. Z., Lu, B., Zhang, C. C., Zhou, J., et al. (2016a). Geological characteristics of source rock and reservoir of tight oil and its accumulation mechanism: A case study of Permian Lucaogou Formation in Jimusar sag, Junggar Basin. *Pet. explor. Dev+* 43 (6), 1013–1024. doi:10.1016/s1876-3804(16)30118-5

Qiu, Z., Tao, H. F., Lu, B., Chen, Z. H., Wu, S. T., Liu, H. L., et al. (2021). Controlling factors on organic matter accumulation of marine shale across the Ordovician-Silurian transition in South China: Constraints from trace-element geochemistry. *J. Earth Sci-China* 32 (4), 887–900. doi:10.1007/s12583-020-1359-x

Qiu, Z., Tao, H. F., Zou, C. N., Wang, H. Y., Ji, H. J., and Zhou, S,X. (2016b). Lithofacies and organic geochemistry of the Middle Permian Lucaogou Formation in the Jimusar Sag of the Junggar Basin, NW China. *J. Pet. Sci. Eng.* 140, 97–107. doi:10.1016/j.petrol.2016.01.014

Qu, C. S., Qiu, L. W., Cao, Y. C., Yang, Y. Q., and Yu, K. H. (2019). Sedimentary environment and the controlling factors of organic-rich rocks in the Lucaogou Formation of the Jimusar Sag, Junggar Basin, NW China. *Pet. Sci.* 16 (4), 763–775. doi:10.1007/s12182-019-0353-3

Qu, J. X., Ding, X. J., Zha, M., Chen, H., Gao, C. H., and Wang, Z. M. (2017). Geochemical characterization of Lucaogou Formation and its correlation of tight oil accumulation in Jimsar Sag of Junggar Basin, Northwestern China. *J. Pet. Explor. Prod. Te.* 7, 699–706. doi:10.1007/s13202-017-0335-1

Ren, J. L., Jin, J., Xiang, B. L., Ma, W. Y., Zhou, N., and Liao, J. D. (2019). Differences and Genesis of shale oil properties between the upper and lower sections of the Lucaogou Formation in the Jimsar Sag. *IOP Conf. Ser. Earth Environ. Sci.* 360 (1), 012032. doi:10.1088/1755-1315/360/1/012032

Renard, S., Pironon, J., Sterpenich, J., Carpentier, C., Lescanne, M., and Gaucher, E. C. (2019). Diagenesis in Mesozoic carbonate rocks in the North Pyrénées (France) from mineralogy and fluid inclusion analysis: Example of Rousse reservoir and caprock. *Chem. Geol.* 508, 30–46. doi:10.1016/j.chemgeo.2018.06.017

Renaut, R. W., Jones, B., Tiercelin, J. J., and Tarits, C. (2002). Sublacustrine precipitation of hydrothermal silica in rift lakes: evidence from Lake Baringo, central Kenya Rift Valley. *Sediment. Geol.* 148 (1-2), 235–257. doi:10.1016/s0037-0738(01)00220-2

Renaut, R. W., Owen, R. B., Lowenstein, T. K., De Cort, G., Mcnulty, E., Scott, J. J., et al. (2021). The role of hydrothermal fluids in sedimentation in saline alkaline lakes: Evidence from Nasikie Engida, Kenya Rift Valley. *Sedimentology* 68 (1), 108–134. doi:10.1111/sed.12778

Rickard, D. (2019). Sedimentary pyrite framboid size-frequency distributions: A meta-analysis. *Palaeogeogr. Palaeoclimatol. Palaeoecol.* 522, 62–75. doi:10.1016/j.palaeo.2019.03.010

Rimmer, S. M., Thompson, J. A., Goodnight, S. A., and Robl, T. L. (2004). Multiple controls on the preservation of organic matter in Devonian-Mississippian marine black shales: geochemical and petrographic evidence. *Palaeogeogr. Palaeoclimatol. Palaeoecol.* 215 (1-2), 125–154. doi:10.1016/s0031-0182(04)00466-3

Rubinstein, N. A., and Carrasquero, S. I. (2019). Petrogenesis of the Triassic Cuyo basin magmatism: Controls on the magmatic evolution of passive rifts basins in Western Gondwana. *J. S. Am. Earth. Sci.* 92, 586–597. doi:10.1016/j.jsames.2019.03.017

Shang, F., Liu, Z. J., Xie, X. N., and Chen, H. (2015). Organic matter accumulation mechanisms of shale series in He-third Member of Eocene Hetaoyuan Formation, Biyang Depression, Eastern China. *Pet. Sci. Technol.* 33, 1434–1442. doi:10.1080/10916466.2015.1075037

Sherman, L. S., Blum, J. D., Nordstorm, D. K., McCleskey, R. B., Barkay, T., and Vetriani, C. (2009). Mercury isotopic composition of hydrothermal systems in the Yellowstone Plateau volcanic field and Guaymas Basin sea-floor rift. *Earth. Planet. Sc. Lett.* 279 (1-2), 86–96. doi:10.1016/j.epsl.2008.12.032

Shu, L. S., Wang, B., Zhu, W. B., Guo, Z. J., Charvet, J., and Zhang, Y. (2011). Timing of initiation of extension in the Tianshan, based on structural, geochemical and geochronological analyses of bimodal volcanism and olistostrome in the Bogda Shan (NW China). *Int. J. Earth. Sci-China* 100, 1647–1663. doi:10.1007/s00531-010-0575-5

Song, J., Bao, Z. D., Zhao, X. M., Gao, Y. S., Song, Y. M., Zhu, Y. Z., et al. (2018). Sedimentology and geochemistry of Middle–Upper Permian in northwestern Turpan–Hami Basin, China: Implication for depositional environments and petroleum geology. *Energy explor. Exploit.* 36 (4), 910–941. doi:10.1177/0144598718779100

Stashchuk, M. F. (1972). “Conditions for formation of iron minerals during sedimentation and diagenesis,” in *The oxidation-reduction potential in geology* (Consultants Bureau), 81–107.

Steinke, S., Kienast, M., and Hanebuth, T. (2003). On the significance of sea-level variations and shelf paleo-morphology in governing sedimentation in the southern South China Sea during the last deglaciation. *Mar. Geol.* 201 (1-3), 179–206. doi:10.1016/s0025-3227(03)00216-0

Su, Y., Zha, M., Ding, X. J., Qu, J. X., Gao, C. H., Jin, J. H., et al. (2019). Petrographic, palynologic and geochemical characteristics of source rocks of the Permian Lucaogou Formation in Jimsar Sag, Junggar Basin, NW China: Origin of organic matter input and depositional environments. *J. Pet. Sci. Eng.* 183, 106364. doi:10.1016/j.petrol.2019.106364

Sun, F. N., Hu, W. X., Cao, J., Wang, X. L., Zhang, Z. R., Ramezani, J., et al. (2022). Sustained and intensified lacustrine methane cycling during Early Permian climate warming. *Nat. Commun.* 13, 4856. doi:10.1038/s41467-022-32438-2

Sun, T., Wang, C. S., Li, Y. L., Wang, L. C., and He, J. L. (2013). Geochemical investigation of lacustrine oil shale in the Lunpola Basin (Tibet): Implications for paleoenvironment and paleoclimate. *Oil shale* 30 (2), 101–116. doi:10.3176/oil.2013.2.02

Tan, J. Q., Wang, Z. H., Wang, W. H., Hilton, J., Guo, J. H., and Wang, X. K. (2021). Depositional environment and hydrothermal controls on organic matter enrichment in the lower Cambrian Niutitang shale, southern China. *AAPG Bull.* 105 (7), 1329–1356. doi:10.1306/12222018196

Tang, W. B., Zhang, Y. Y., Pe-Piper, G., Piper, D. J. W., Guo, Z. J., and Li, W. (2021). Permian to early Triassic tectono-sedimentary evolution of the Mahu sag, Junggar Basin, Western China: sedimentological implications of the transition from rifting to tectonic inversion. *Mar. Pet. Geol.* 123, 104730. doi:10.1016/j.marpetgeo.2020.104730

Tao, H. F., Qiu, Z., Qu, Y. Q., Liu, J., Qin, Z., Xie, Z. B., et al. (2022). Geochemistry of Middle Permian Lacustrine shales in the Jimusar Sag, Junggar Basin, NW China: Implications for hydrothermal activity and organic matter enrichment. *J. Asian. Earth. Sci.* 232, 105267. doi:10.1016/j.jseaes.2022.105267

Tao, S., Wang, Y. B., Tang, D. Z., Wu, D. M., Xu, H., and He, W. (2012). Organic petrology of Fukang Permian Lucaogou Formation oil shales at the northern foot of Bogda Mountain, Junggar Basin, China. *Int. J. Coal. Geol.* 99, 27–34. doi:10.1016/j.coal.2012.05.001

Tao, S., Xu, Y. B., Tang, D. Z., Xu, H., Li, S., Chen, S. D., et al. (2017). Geochemistry of the Shitoumei oil shale in the Santanghu Basin, Northwest China: Implications for paleoclimate conditions, weathering, provenance and tectonic setting. *Int. J. Coal. Geol.* 184, 42–56. doi:10.1016/j.coal.2017.11.007

Tessin, A., Chappaz, A., Hendy, I., and Sheldon, N. (2019). Molybdenum speciation as a paleo-redox proxy: A case study from Late Cretaceous Western Interior Seaway black shales. *Geology* 47 (1), 59–62. doi:10.1130/g45785.1

Thomson, J., Jarvis, I., Green, D. R. H., Green, D. A., and Clayton, T. (1998). Mobility and immobility of redox-sensitive elements in deep-sea turbidites during shallow burial. *Geochim. Cosmochim. Ac.* 62 (4), 643–656. doi:10.1016/s0016-7037(97)00378-5

Tian, S. Y., Yasuhara, M., Robinson, M. M., and Huang, H. M. (2022). Ostracod eye size: A taxonomy-free indicator of the Paleocene-Eocene Thermal Maximum sea level. *Mar. Micropaleontol.* 174, 101994. doi:10.1016/j.marmicro.2021.101994

Tourtelot, H. A. (1979). Black Shale-Its Deposition and Diagenesis. *Clay. Clay. Min.* 27, 313–321. doi:10.1346/ccmn.1979.0270501

Vovk, I. F. (1987). “Some geochemical and mineralogical pecularities of deposits of radioactive materials as evidence for radiolysis in nature,” in *Natural analogues in radioactive waste disposal*. Editors B. Come, and N. A. Chapman (Dordrecht: Graham & Trotman), 205–216.

Wang, J. L., Wu, C. D., Jiao, Y., and Yuan, B. (2021). Middle-Late Triassic sedimentary provenance of the southern Junggar Basin and its link with the post-orogenic tectonic evolution of Central Asia. *Sci. Rep-UK* 11 (1), 17041. doi:10.1038/s41598-021-96455-9

Wang, J. L., Wu, C. D., Li, Z., Zhu, W., Zhou, T. Q., Wu, J., et al. (2018a). The tectonic evolution of the Bogda region from late Carboniferous to Triassic time: evidence from detrital zircon U-Pb geochronology and sandstone petrography. *Geol. Mag.* 155 (5), 1063–1088. doi:10.1017/s0016756816001217

Wang, J. L., Wu, C. D., Li, Z., Zhu, W., Zhou, T. Q., Wu, J., et al. (2018b). Whole-rock geochemistry and zircon Hf isotope of Late Carboniferous-Triassic sediments in the Bogda region, NW China: Clues for provenance and tectonic setting. *Geol. J.* 54 (4), 1853–1877. doi:10.1002/gj.3110

Wang, J. L., Wu, C. D., Zhou, T. Q., Zhu, W., Li, X. Y., and Zhang, T. (2019a). Source and sink evolution of a Permian-Triassic rift-drift basin in the southern Central Asian Orogenic Belt: Perspectives on sedimentary geochemistry and heavy mineral analysis. *J. Asian. Earth. Sci.* 181, 103905. doi:10.1016/j.jseaes.2019.103905

Wang, J. L., Wu, C. D., Zhou, T. Q., Zhu, W., Zhou, Y. X., Jiang, X., et al. (2019b). Source-to-Sink Analysis of a Transtensional Rift Basin from Syn-Rift to Uplift Stages. *J. Sediment. Res.* 89, 335–352. doi:10.2110/jsr.2019.19

Wang, M., Guo, Z. Q., Jiao, C. X., Lu, S. F., Li, J. B., Xue, H. T., et al. (2019c). Exploration progress and geochemical features of lacustrine shale oils in China. *J. Pet. Sci. Eng.* 178, 975–986. doi:10.1016/j.petrol.2019.04.029

Wang, M., Xue, H. T., Tian, S. S., Wilkins, R. W. T., and Wang, Z. W. (2015). Fractal characteristics of Upper Cretaceous lacustrine shale from the Songliao Basin, NE China. *Mar. Pet. Geol.* 67, 144–153. doi:10.1016/j.marpetgeo.2015.05.011

Wang, Q. F., Jiang, F. J., Ji, H. C., Jiang, S., Liu, X. H., Zhao, Z., et al. (2020a). Effects of paleosedimentary environment on organic matter enrichment in a saline lacustrine rift basin - A case study of Paleogene source rock in the Dongpu Depression, Bohai Bay Basin. *J. Pet. Sci. Eng.* 195, 107658. doi:10.1016/j.petrol.2020.107658

Wang, Y. C., Cao, J., Tao, K. Y., Li, E. T., Ma, C., and Shi, C. H. (2020b). Reevaluating the source and accumulation of tight oil in the middle Permian Lucaogou Formation of the Junggar Basin, China. *Mar. Pet. Geol.* 117, 104384. doi:10.1016/j.marpetgeo.2020.104384

Wang, Y. C., Cao, J., Tao, K. Y., Xiao, W. Y., Xiang, B. L., Li, E. T., et al. (2022). Absence of β-carotane as proxies of hydrothermal activity in brackish lacustrine sediments. *Palaeogeogr. Palaeoclimatol. Palaeoecol.* 587, 110801. doi:10.1016/j.palaeo.2021.110801

Wang, Z. W., Wang, J., Fu, X. G., Feng, X. L., Armstrong-Altin, J. S., Zhan, W. Z., et al. (2019d). Sedimentary successions and onset of the Mesozoic Qiangtang rift basin (northern Tibet), Southwest China: Insights on the Paleo- and Meso-Tethys evolution. *Mar. Pet. Geol.* 102, 657–679. doi:10.1016/j.marpetgeo.2019.01.017

Wei, W., and Algeo, T. J. (2020). Elemental proxies for paleosalinity analysis of ancient shales and mudrocks. *Geochim. Cosmochim. Ac.* 287, 341–366. doi:10.1016/j.gca.2019.06.034

Wei, Z. F., Wang, Y. L., Wang, G., Zhang, T., He, W., Ma, X. Y., et al. (2020). Enrichment Mechanism of the Upper Carboniferous-Lower Permian Transitional Shale in the East Margin of the Ordos Basin, China: Evidence from Geochemical Proxies. *Geofluids* 2020, 1–14. doi:10.1155/2020/8867140

Wu, H. G., Hu, W. X., Cao, J., Wang, X. L., Wang, X. L., and Liao, Z. W. (2016). A unique lacustrine mixed dolomitic-clastic sequence for tight oil reservoir within the middle Permian Lucaogou Formation of the Junggar Basin, NW China: Reservoir characteristics and origin. *Mar. Pet. Geol.* 76, 115–132. doi:10.1016/j.marpetgeo.2016.05.007

Wu, H. G., Zhou, J. J., Hu, W. X., Sun, F. N., Kang, X., Zhang, Y. F., et al. (2022). Origin of authigenic albite in a lacustrine mixed-deposition sequence (Lucaogou Formation, Junggar Basin) and its diagenesis implications. *Energy explor. Exploit.* 40 (1), 132–154. doi:10.1177/01445987211042702

Wu, S. T., Zhai, X. F., Yang, Z., Bale, H., Hong, Y. L., Cui, J. W., et al. (2019). Characterization of fracture formation in organic-rich shales - An experimental and real time study of the Permian Lucaogou Formation, Junggar Basin, northwestern China. *Mar. Pet. Geol.* 102, 397–406. doi:10.1016/j.marpetgeo.2019.05.036

Xie, X. M., Borjigin, T., Zhang, Q. Z., Zhang, Z. R., Qin, J. Z., Bian, L. Z., et al. (2015). Intact microbial fossils in the Permian Lucaogou Formation oil shale, Junggar Basin, NW China. *Int. J. Coal. Geol.* 146, 166–178. doi:10.1016/j.coal.2015.05.011

Xie, X. M., Zhu, G. Y., and Wang, Y. (2021). The influence of syngenetic hydrothermal silica fluid on organic matter preservation in lower Cambrian Niutitang Formation, South China. *Mar. Pet. Geol.* 129, 105098. doi:10.1016/j.marpetgeo.2021.105098

Xu, Z. J., Wang, Y., Jiang, S., Fang, C., Liu, L. F., Wu, K. J., et al. (2021). Impact of input, preservation and dilution on organic matter enrichment in lacustrine rift basin: A case study of lacustrine shale in Dehui Depression of Songliao Basin, NE China. *Mar. Pet. Geol.* 135 (3), 105386. doi:10.1016/j.marpetgeo.2021.105386

Yang, G. Q., Zeng, J. H., Qiao, J. C., Liu, Y. Z., Cao, W. F., Wang, C. Y., et al. (2022). Differences between laminated and massive shales in the Permian Lucaogou Formation: Insights into the paleoenvironment, petrology, organic matter and microstructure. *Acs. Earth. Space. Chem.* 6 (10), 2530–2551. doi:10.1021/acsearthspacechem.2c00245

Yang, Y. Q., Qiu, L. W., Wan, M., Jia, X. Y., Cao, Y. C., Lei, D. W., et al. (2019a). Depositional model for a salinized lacustrine basin: The Permian Lucaogou Formation, Jimsar Sag, Junggar Basin, NW China. *J. Asian. Earth. Sci.* 178, 81–95. doi:10.1016/j.jseaes.2018.08.021

Yang, Z., Zhong, D. K., Whitaker, F., Lu, Z., Zhang, S., Tang, Z. C., et al. (2020). Syn-sedimentary hydrothermal dolomites in a lacustrine-rift basin: Petrographic and geochemical evidence from the lower Cretaceous Erlian Basin, Northern China. *Sedimentology* 67 (1), 305–329. doi:10.1111/sed.12644

Yang, Z., Zou, C. N., Hou, L. H., Wu, S. T., Lin, S. H., Luo, X., et al. (2019b). Division of fine-grained rocks and selection of "sweet sections" in the oldest continental shale in China: Taking the coexisting combination of tight and shale oil in the Permian Junggar Basin. *Mar. Pet. Geol.* 109, 339–348. doi:10.1016/j.marpetgeo.2019.06.010

You, J. Y., Liu, Y. Q., Li, Y. J., Zhou, D. W., Zheng, Q. H., Yang, Y. Y., et al. (2021). Influencing factor of Chang 7 oil shale of Triassic Yanchang Formation in Ordos Basin: Constraint from hydrothermal fluid. *J. Pet. Sci. Eng.* 201, 108532. doi:10.1016/j.petrol.2021.108532

Yu, K. H., Qiu, L. W., Cao, Y. C., Sun, P. P., Qu, C. S., and Yang, Y. Q. (2019). Hydrothermal origin of early Permian saddle dolomites in the Junggar Basin, NW China. *J. Asian. Earth. Sci.* 184, 103990. doi:10.1016/j.jseaes.2019.103990

Yu, Y. L., Wang, X., Rao, G., and Wang, R. F. (2016). Mesozoic reactivated transpressional structures and multi-stage tectonic deformation along the Hong-Che fault zone in the northwestern Junggar Basin, NW China. *Tectonophysics* 679 (4), 156–168. doi:10.1016/j.tecto.2016.04.039

Zeng, Z. G., Ouyang, H. G., Yin, X. B., Chen, S., Wang, X. Y., and Wu, L. (2012). Formation of Fe-Si-Mn oxyhydroxides at the PACMANUS hydrothermal field, Eastern Manus Basin: Mineralogical and geochemical evidence. *J. Asian. Earth. Sci.* 60, 130–146. doi:10.1016/j.jseaes.2012.08.009

Zha, X. J., Lai, F. Q., Gao, X. B., Gao, Y., Jiang, N., Luo, L., et al. (2021). Characteristics and genetic mechanism of pore throat structure of shale oil reservoir in saline lake - A case study of shale oil of the Lucaogou Formation in Jimsar Sag, Junggar Basin. *Energies* 14, 8450. doi:10.3390/en14248450

Zhang, J. Y., Sun, M. L., Liu, G. D., Cao, Z., and Kong, Y. H. (2020a). Geochemical Characteristics, Hydrocarbon Potential, and Depositional Environment Evolution of Fine-Grained Mixed Source Rocks in the Permian Lucaogou Formation, Jimusaer Sag, Junggar Basin. *Energy Fuel.* 35 (1), 264–282. doi:10.1021/acs.energyfuels.0c02500

Zhang, K., Liu, R., Liu, Z. J., Li, B. L., Han, J. B., and Zhao, K. G. (2020b). Influence of volcanic and hydrothermal activity on organic matter enrichment in the Upper Triassic Yanchang Formation, southern Ordos Basin, Central China. *Mar. Pet. Geol.* 112, 104059. doi:10.1016/j.marpetgeo.2019.104059

Zhang, M. M., and Li, Z. (2018a). Thermal maturity of the Permian Lucaogou Formation organic-rich shale at the northern foot of Bogda Mountains, Junggar Basin (NW China): Effective assessments from organic geochemistry. *Fuel* 211, 278–290. doi:10.1016/j.fuel.2017.09.069

Zhang, M. M., Li, Z., and Yin, J. (2018b). Sedimentary and geochemical characteristics of oil shale in the Permian Lucaogou Formation in the southeastern Junggar Basin, northwest China: Implications for sedimentary environments. *Oil Shale* 35 (2), 97–112. doi:10.3176/oil.2018.2.01

Zhang, M. M., Liu, Z. J., Qiu, H. J., and Xu, Y. B. (2016). Characteristics of organic matter of Oil shale in the Sequence stratigraphic framework at the northern foot of Bogda Mountain, China. *Oil Shale* 33 (1), 31–44. doi:10.3176/oil.2016.1.03

Zhang, M. M., Liu, Z. J., Xu, S. Z., Hu, X. F., Sun, P. C., and Wang, Y. L. (2014). Analysis for the Paleosalinity and Lake-level Changes of the Oil Shale Measures in the Lucaogou Formation in the Sangonghe Area of Southern Margin, Junggar Basin. *Pet. Sci. Technol.* 32, 1973–1980. doi:10.1080/10916466.2012.742541

Zhang, S. H., Liu, C. Y., Liang, H., Jia, L. B., Bai, J. K., Zhang, L., et al. (2021). Mineralogical composition and organic matter characteristics of lacustrine fine-grained volcanic-hydrothermal sedimentary rocks: A data-driven analytics for the second member of Permian Lucaogou Formation, Santanghu Basin, NW China. *Mar. Pet. Geol.* 126, 104920. doi:10.1016/j.marpetgeo.2021.104920

Zhang, S. H., Liu, C. Y., Liang, H., Wang, J. Q., Bai, J. K., Yang, M. H., et al. (2018c). Paleoenvironmental conditions, organic matter accumulation, and unconventional hydrocarbon potential for the Permian Lucaogou Formation organic-rich rocks in Santanghu Basin, NW China. *Int. J. Coal. Geol.* 185, 44–60. doi:10.1016/j.coal.2017.11.012

Zhang, S. H., Wang, J. Q., Liu, C. Y., Bai, J. K., Peng, H., Huang, H. X., et al. (2018d). Detrital zircon U-Pb geochronology of the Permian strata in the Turpan-Hami Basin in North Xinjiang, NW China: Depositional age, provenance, and tectonic implications. *Geol. J.* 54 (2), 1064–1080. doi:10.1002/gj.3374

Zhang, S., Liu, Y. Q., Li, H., Jiao, X., and Zhou, D. W. (2020c). Hydrothermal-sedimentary dolomite-a case from the Middle Permian in eastern Junggar Basin, China. *J. Palaeogeog-English* 9 (1), 24–23. doi:10.1186/s42501-020-00070-0

Zhang, S. M., Cao, Y. C., Liu, K. Y., Jahren, J., Xi, K. L., Zhu, R. K., et al. (2019a). Characterization of lacustrine mixed fine-grained sedimentary rocks using coupled chemostratigraphic-petrographic analysis: A case study from a tight oil reservoir in the Jimusar Sag, Junggar Basin. *Mar. Pet. Geol.* 99, 453–472. doi:10.1016/j.marpetgeo.2018.10.039

Zhang, X. Y., Li, S. J., Zhao, X. L., Geng, G., and Yan, M. M. (2020d). The sedimentary environment of Early Cretaceous rift basin in eastern China and its response to the Faraoni event. *Geosci. J.* 24 (4), 359–377. doi:10.1007/s12303-019-0031-x

Zhang, Y., Horsfield, B., Hou, D. J., Noah, M., and Yang, S. Y. (2019b). Impact of hydrothermal activity on organic matter quantity and quality during deposition in the Permian Dalong Formation, Southern China. *Mar. Pet. Geol.* 110, 901–911. doi:10.1016/j.marpetgeo.2019.08.049

Zhang, Y., Li, Z. S., Nie, F., Tian, X. L., and Shi, Y. H. (2015). Age, provenance and tectonic evolution of Late Paleozoic strata in Bogda Mountain, Xinjiang: Evidence from detrital zircon U-Pb geochronology. *Chin. J. Geol.* 50 (1), 155–181. (In Chinese with English Abstract).

Zhao, P. Q., Wang, Z. L., Sun, Z. C., Cai, J. C., and Wang, L. (2017). Investigation on the pore structure and multifractal characteristics of tight oil reservoirs using NMR measurements: Permian Lucaogou Formation in Jimusaer Sag, Junggar Basin. *Mar. Pet. Geol.* 86, 1067–1081. doi:10.1016/j.marpetgeo.2017.07.011

Zhao, R., Zhang, J. Y., Zhou, C. M., Zhang, Z. J., Chen, S., Stockli, D. F., et al. (2020a). Tectonic evolution of Tianshan-Bogda-Kelameili mountains, clastic wedge basin infill and chronostratigraphic divisions in the source-to-sink systems of Permian-Jurassic, southern Junggar Basin. *Mar. Pet. Geol.* 114, 104200. doi:10.1016/j.marpetgeo.2019.104200

Zhao, W. Z., Hu, S. Y., Hou, L. H., Yang, t., li, X., Guo, B. C., et al. (2020b). Types and resource potential of continental shale oil in China and its boundary with tight oil. *Pet. explor. Dev+* 47 (1), 1–11. doi:10.1016/s1876-3804(20)60001-5

Zheng, R. H., Zhang, G. L., Qu, Y. S., Wang, S. Z., Jin, X., Chen, X., et al. (2022). Oil-source correlation under the complex geological conditions: A case study of the Chaiwopu Sag, southern Junggar Basin, NW China. *J. Pet. Sci. Eng.* 210, 110056. doi:10.1016/j.petrol.2021.110056

Zou, C. N., Zhu, R. K., Chen, Z. Q., Ogg, J. G., Wu, S. T., Dong, D. Z., et al. (2019). Organic-matter-rich shales of China. *Earth-Sci. Rev.* 189, 51–78. doi:10.1016/j.earscirev.2018.12.002